Coherent Anti-Stokes Raman Spectroscopy of Diamond

Narendra Balaguru Viranna

This thesis is submitted in fulfilment
of the requirements of the degree of
Master of Science

DEPARTMENT OF PHYSICS
UNIVERSITY OF CAPE TOWN

March 1997

Abstract

Experiments were performed to investigate Coherent Anti-Stokes Raman Scattering (CARS) in diamond. Aspects of this type of non-linear scattering are presented theoretically, and various experimental configurations were attempted in order to study them. These included the dependence of the CARS signal intensity on the intensities of the two exciting frequency-doubled Nd:YAG (pump) and dye (Stokes) lasers, the variation of the CARS signal polarization as a function of the lasers' polarization, and the dependence of the CARS signal intensity on the phase mismatch of the laser beams. The phase mismatch measurement confirmed the predicted sinc^2 nature of the CARS signal intensity, while the polarization measurements provided new information on the ratio of the non-vanishing components of the cubic susceptibility χ^3 of diamond. The CARS signal intensity was found to change linearly with the dye laser intensity and quadratically with the Nd:YAG laser intensity. The CARS signal was found at the predicted 1332 cm^{-1} shift from the doubled Nd:YAG emission, and its linewidth of 1.2 cm^{-1} is in agreement with the spontaneous Raman linewidth.The spectral data were fitted to a modified Voigt profile containing the non-resonant cubic susceptibility contribution, and this allowed us to establish the ratio of the resonant and non-resonant parts of χ^3. An attempt to generate Stimulated Raman Scattering in diamond was unsuccessful.

Table of Contents

Chapter 1

Introduction

When light of a given frequency is incident on a material medium, one finds that the scattered light contains not only the frequency of the incident light, but other frequencies also. This phenomenon whereby the scattered radiation is different in frequency is called Raman scattering, after C.V. Raman and K.S. Krishnan[1] who were the first to observe this type of scattering. This was in 1928 and involved the use of a powerful beam of focused sunlight to illuminate different liquids. The change in frequency that is observed is related to the vibrational, rotational or electronic energy levels of the medium under consideration.

Many forms of Raman scattering exist, all identifiably by the shift in frequency of the scattered light. They are an invaluable tool for the spectroscopist since Raman spectroscopy allows dipole transitions, normally forbidden due to parity restrictions, to be accessed. Thus the group of Raman spectroscopies allow us to examine molecular structure that would otherwise be very difficult or impossible to observe. Conventional linear or spontaneous Raman scattering however has some inherent difficulties. First, the molecular system under consideration sometimes displays fluorescence in the region of the spontaneous Raman signal, and the rejection of this fluorescence requires careful experimental planning (for example the use of a fourier transform Raman spectrometer), bring with it additional difficulties. Secondly, the typical small scattering cross sections result in the intensity of the detected radiation being very weak. This is exacerbated by the isotropic nature of spontaneous Raman scattering, which allows for only a tiny fraction of the total scattered light to be collected for analysis.

Brighter sources of illumination increase the collected signal intensity, and in this regard the progress made in laser technology in providing high power, monochromatic sources of light has spurred on the application of Raman spectroscopy. Pulsed lasers providing gigawatts of peak power and tunable lasers allowing the wavelength of light to be readily selected, have opened up the field of optical spectroscopy and allowed non-linear effects to be investigated. Of the many non-linear optical techniques that exist, we are interested in the coherent Raman effect known as Coherent Anti-Stokes Raman Scattering (CARS). The acronym CARS is also used to refer to Coherent Anti-Stokes Raman Spectroscopy.

CARS is a four-wave mixing process where three waves are coupled to produce coherent radiation at a frequency higher than any of the input electric fields' frequencies. It was first observed more than three decades ago by Maker and Terhune[2], who considered the theoretical implication of a medium's polarization taking on a non-linear resonant nature, and performed experiments to show that the effects predicted by these calculations, exist. The third-order polarization term then involves the coupling of the third-order electric susceptibility $\chi^{(3)}$, to three electric fields. It is this bulk material property which gives rise to CARS, as well as other non-linear phenomena such as saturation spectroscopy, two-photon absorption, and stimulated Raman gain or loss spectroscopy. The fact that CARS is a coherent non-linear laser spectroscopic technique means that it is more complex experimentally and in mechanism, but it has the benefit of allowing additional structural and state information to be gathered through the inelastic scattering of light, than spontaneous Raman spectroscopy.

CARS overcomes the above-mentioned problems associated with spontaneous Raman scattering in that very high signal levels and greater signal to noise ratios, usually orders of magnitude larger than in the spontaneous case, are achieved. Furthermore, since the CARS signal has a small divergence, collection efficiencies are greatly increased and excellent spatial discrimination of the CARS signal from background radiation as well as the input lasers' radiation is possible. Also, the problem with fluorescence is eliminated since the signal is an anti-Stokes one, i.e. the signal has a frequency higher than any of the input lasers' frequencies. Making use of CARS, one can also map temperature and fractional species concentrations of a gas, to a spatial resolution limited only by the beam profile and

power of the lasers being used, as well as investigate molecular rotational states that are not observed in spontaneous Raman spectroscopy due to their small signal strengths.

The major disadvantages with CARS include the presence of a non-Raman resonant background which interferes with the resonant CARS lineshapes making detection of weak signals and analysis of all signals arduous. A further complexity in obtaining a CARS signal is brought about by the requirement for phase matching or momentum conservation. This involves allowing three or two (in the degenerate case) laser beams to intersect at the appropriate angles(s). This is especially true in condensed phases where the index of refraction is strongly dispersive. The equipment used is also more expensive than for spontaneous Raman spectroscopy, as two or three high power lasers are needed.

The majority of the work performed in the CARS field has been in the gas phase, particularly in combustion diagnostics[3,4]. This is due to the ability of CARS to probe, in a non-intrusive manner, hot reactive gases in hostile, rapidly changing systems and provide spatial state information such as temperature, pressure and velocity as well as structural information in the form of species concentrations. Low-pressure gases and plasmas have also been studied, and ultra-high resolution spectra of gases[5,6] obtained using CARS.

The motivation to investigate CARS in diamond comes from the fact that little current work has been performed in the condensed phase. In 1972 Levenson, Flytzanis and Bloembergen[7] performed the first CARS experiment in diamond, followed by a more thorough investigation of centrosymmetric media two years later by Levenson and Bloembergen[8]. The improvement in laser technology in the ensuing time led us to believe that with the pulsed, high power, single longitudinal mode, frequency-doubled Nd:YAG and tunable dye lasers at our disposal, spectral details not observed by these authors might be seen by us. Diamond is an ideal candidate for investigation, since it is an optically transparent, cubic crystal with a high index of refraction. Its centrosymmetric nature means that the analysis in terms of the lasers' polarizations is relatively simple, and its high refractive index allow the phase matching aspects of CARS to be properly studied.

An online literature search of physics and chemical physics electronic databases revealed that the only major study of CARS from diamond has been the above-mentioned work by Levenson, Bloembergen and Flytzanis. They reported the observation of a CARS signal from diamond, calculated values for the Raman shift and the linewidth, but concentrated mainly on determining the tensor components of the non-resonant contribution to the cubic susceptibility. This work has been reviewed and quoted by some authors[9,10,11,12,13]. Titkov *et al.*[14], recently reported a CARS experiment in brown diamonds, where a new Raman line slightly below that of the conventional line, was observed. They ascribed this new line to the large number of dislocations and plastic deformations found in their crystals. Other effects resulting from the coupling of radiation with the cubic susceptibility in diamond have been reported.

Our investigation of CARS in diamond was experimental in nature, testing documented theoretical aspects. The results obtained agree favourably with CARS theory. The principle novel measurement performed by us is that of the ratio of the cubic susceptibility tensor components, and estimates for the non-resonant background as a function of laser polarization. We also present experimental confirmation of the phase matching dependence, on the angle of intersection of the laser beams.

Chapter 2 comprises an overview of the basic CARS theory, where the process is first described, before expressions for the intensity and non-linear susceptibility are presented, together with outlines of their derivations. The derivations use Maxwell's electromagnetic theory, quantum mechanics, and some classical mechanics. The resonant nature of the CARS process is revealed, as is the interference between the resonant and non-resonant parts of the cubic electric susceptibility.

In Chapter 3, details of the equipment used in this study are provided. This includes a description of the laser system, the spectrometer, and the various experimental configurations used. Aspects of diamond affecting the equipment and these setups are also discussed, as are the workings of the Fabry Perot étalons used to ensure single longitudinal mode operation of the Nd:YAG laser.

Chapter 4 describes the experiments performed, the procedure followed in each, their results, and were applicable, comparison the other work performed on diamond in this field.

Finally, chapter 5 summarises all the work done, and provides a few concluding remarks and suggestions.

All numerical calculations in this work were performed on a computer using the Quattro Pro Spreadsheet program for basic calculations and initial rendering of graphs, a demonstration version of the Microcal Origin program for curve fitting where the Levenberg-Marquardt algorithm was employed, and Harvard Graphics for final diagrams and graphs.

Chapter 2

Theory

This chapter presents an overview of CARS theory, focusing on aspects deemed to be important for this work. Detailed reviews have been written by Levenson and Kano[10], Greenhalgh[3], Druet and Taran[5], and Nibler and Knighten[15] to name a few authors. We first present a generalised description of the CARS mechanism making use of an energy level transition model, before deriving an equation for the CARS signal intensity and an expression for the electric susceptibility. The response of the medium is expressed in terms of its various tensor susceptibilities, and through Maxwell's equations the optical response is established in terms of the signal intensity. Quantum mechanics allows the susceptibility and the microscopic nature of the molecules to be connected in terms of molecular wave functions and ensemble averages. Various aspects important to the technique, and which ensure its uniqueness, are discussed as they make themselves evident.

2.1 General description

Qualitatively, CARS can be understood as arising, as in spontaneous linear Raman scattering, out of the polarization $\boldsymbol{P}$ and therefore the susceptibility χ. In a dielectric material, the induced polarization due to large applied electric fields can be expressed as a power series

$$\begin{aligned} \boldsymbol{P} &= \boldsymbol{P}^{(1)} + \boldsymbol{P}^{(2)} + \boldsymbol{P}^{(3)} + \ldots \\ \therefore\ P_i &= \chi^{(1)}_{ij} E_j + \chi^{(2)}_{ijk} E_j E_k + \chi^{(3)}_{ijkl} E_j E_k E_l + \ldots, \end{aligned} \tag{1}$$

where $\chi^{(n)}$ is the susceptibility tensor of rank (n + 1). The spontaneous Raman scattered signal arises from the interaction of the incident E_j electric field with the linear susceptibility $\chi^{(1)}$. A Raman process describes the interaction of one or more applied fields with the dipole

moment of a medium, resulting in scattered radiation whose frequency (and in general polarization) is different from that of the incident field[9]. This frequency difference is termed the Raman shift and is equal to a difference in energy levels, be they vibrational, rotational or electronic, of the molecules under consideration.

In the spontaneous Raman case, one electric field is incident and the radiation is in general predominantly isotropically scattered, with a small anisotropic component. If the scattered radiation has a smaller frequency than that of the incident fields, this is termed Stokes scattering. A Stokes scattered wave is due to the transition of the molecules from a lower to a higher energy level. We visualise the incident photon being annihilated and the scattered photon being created in the transition. When the incident radiation induces the transition of the molecules from this excited state to its original (ground) state, the scattered radiation now has a higher frequency than that of the incident radiation and this is termed anti-Stokes scattering. Again we may visualise the incident photon being annihilated and a photon of higher energy being created.

The CARS signal is due to the third order susceptibility $\chi^{(3)}$. Fig. 1 compares the energies of the incident electric fields with the energy levels of the dielectric medium. This diagram does not define a time-ordering of the energy level transitions, but serves to help us visualise the CARS process. Quantum mechanical perturbation theory allows us to derive a form for the third order susceptibility $\chi^{(3)}$ involving "sequences" of transitions between real and virtual energy states. This will be discussed in more detail later in this chapter (§ 2.4)

Three input electric fields (laser light) of frequency ω_0, ω_1, ω_2 are involved, although two are (usually) degenerate i.e. $\omega_0 = \omega_1$. The terms or transitions responsible for CARS are illustrated in Fig. 1. On a quantum mechanical level, Bloembergen[12], and Druet and Taran[5] state that far from resonance, the CARS process can be described as being parametric, where two photons of frequency ω_1 are destroyed and photons at frequencies ω_2 and ω_3 are created, without energy exchange with the medium. However, near resonance this description is incorrect, and the CARS process must be described as the interference between two "Raman-like" processes. Now the CARS transition is described as an ω_1 photon being absorbed and a ω_2 photon emitted, as well as the absorption of the ω_3 photon and the emission of an ω_1

photon. This difference in description of the CARS process is due to the complex resonant nature of the electric susceptibility, and will be made more obvious after the derivations in § 2.4.

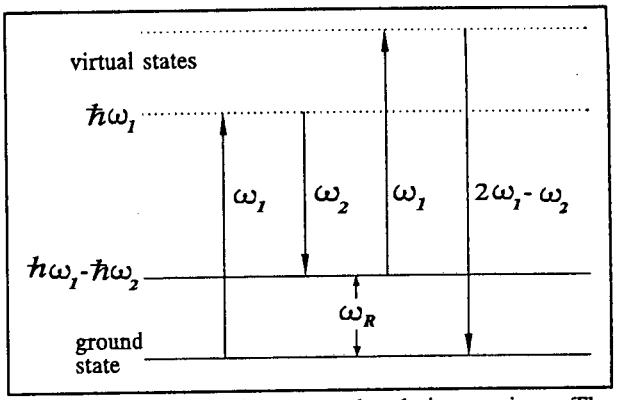

Fig. 1 Schematic of energy level interaction. The broken lines represent virtual states, while the solid lines real energy states. Only energy levels and photon energies are shown, and no time-ordering of the CARS process is implied.

An alternate semi-classical interpretation is also valid, where CARS can be viewed as inelastic scattering from a coherently driven Raman-active molecular vibration. Using the mass on a string model of molecular vibrations, we can interpret the first and second (ω_1 and ω_2) electric fields as coherently driving a vibration of frequency $\omega_1 - \omega_2$. This third (first) ω_1 field then produces an inelastically scattered ω_3 wave of frequency

$$\omega_3 = \omega_1 + (\omega_1 - \omega_2) = 2\omega_1 - \omega_2. \tag{2}$$

This ω_3 radiation is the CARS signal, and therefore has a frequency $\omega_3 = 2\omega_1 - \omega_2$. For CARS, $\omega_2 < \omega_1$ and the measured signal has a greater frequency than either of the lasers, and is therefore an anti-Stokes signal. The related $\omega_2 > \omega_1$ process produces a Stokes (CSRS) signal. Denoting the difference between the ground state and an energy state above ground by ω_R, we see that if $\omega_1 - \omega_2$ corresponds to this difference ω_R, the CARS signal will be resonantly enhanced (see later § 2.4). From Eq. (2), we also note that the CARS frequency ω_3, can be interpreted as a shift in frequency from the ω_1 electric field by a factor $\omega_1 - \omega_2$. Since this shift must equal ω_R for a strong CARS signal, ω_R is termed the Raman shift as in the spontaneous Raman case. It is usually expressed in wavenumbers ν_R, where $\nu_R = \omega_R/(2\pi c)$. Note that ω_2 and ω_3 can be expressed as

$$\omega_2 = \omega_1 - \omega_R, \tag{3}$$

and

$$\omega_3 = \omega_1 + \omega_R. \tag{4}$$

2.2 Classical derivation of signal intensity

2.2.1 Maxwell's equations

It is possible to derive an expression for the CARS signal intensity through a classical approach, coupling Maxwell's relations with a plane wave approximation for the incident electric fields. The form for $\chi^{(3)}$ is then established by means of a quantum-mechanical perturbation of the density operator, or a semi-classical driven lattice mode (photon-phonon) interaction.

Maxwell's equations are the starting point[15,9,10,3,11,6] for describing interactions between electromagnetic waves and matter. They can be written as

$$\begin{aligned} \nabla \cdot \boldsymbol{D} &= \rho_f \qquad & \nabla \times \boldsymbol{E} &= -\frac{\partial \boldsymbol{B}}{\partial t} \\ \nabla \cdot \boldsymbol{B} &= 0 \qquad & \nabla \times \boldsymbol{H} &= \boldsymbol{J}_f + \frac{\partial \boldsymbol{D}}{\partial t}, \end{aligned} \tag{5}$$

where

$$\boldsymbol{D} = \epsilon_0 \boldsymbol{E} + \boldsymbol{P} \qquad \boldsymbol{H} = \frac{\boldsymbol{B}}{\mu_0} - \boldsymbol{M}. \tag{6}$$

In what follows we consider media that are charge free ($\rho_f = 0$), current free ($\boldsymbol{J}_f = 0$) and magnetization free ($\boldsymbol{M} = 0$)[5,15]. Manipulation of the curl equations leads to the wave equation with an induced polarization source term

$$\nabla(\nabla \cdot \boldsymbol{E}) - \nabla^2 \boldsymbol{E} = -\mu_0 \epsilon_0 \frac{\partial^2 \boldsymbol{E}}{\partial t^2} - \mu_0 \frac{\partial^2 \boldsymbol{P}}{\partial t^2}. \tag{7}$$

The plane wave approximation for the induced electric field

$$\boldsymbol{E}(\omega_\alpha, r, t) = \tfrac{1}{2}[\boldsymbol{E}_\alpha(r) e^{i(\boldsymbol{k}_\alpha \cdot r - \omega_\alpha t)} + c.c.], \tag{8}$$

is utilized, where *c.c.* is the complex conjugate, required to ensure that $\boldsymbol{E}$ is real. For isotropic media (gases and liquids), the electric field is transverse to the direction of propagation of the field, so that $\nabla \cdot \boldsymbol{E} = 0$. Armstrong *et al.*[16] show that this assumption of optical isotropy can hold true in cubic crystals with centres of inversion, provided a local field correction is made to the incident electric fields. This requires

$$E_{local} = E + \frac{1}{3}P_{total} = E + \frac{1}{3}P^{(1)} + \frac{1}{3}P^{NL}, \tag{9}$$

where $P^{NL} = P^{(2)} + P^{(3)} + \ldots$, is the nonlinear polarization. The effective nonlinear polarization is then[16,17,18]

$$P^{NL}_{eff} = \frac{(\epsilon + 2)}{3}P^{NL}, \tag{10}$$

and the susceptibility $\chi^{(3)}$ must be adjusted by the factor

$$\prod_{\alpha=1}^{4} \frac{\epsilon(\omega_\alpha) + 2}{3}. \tag{11}$$

We will henceforth incorporate these corrections for the local field into the polarization and cubic susceptibility.

We now assume the one-dimensional case $k = k_z$, and select the electric field polarization so that it contains no component in the z direction, i.e. $E_\alpha(z) = E_x(z)\hat{\imath} + E_y(z)\hat{\jmath}$. Under these approximations $\nabla \cdot P = 0$, implying $\nabla \cdot E = 0$. Assuming further that E_α varies slowly with z so that

$$\frac{\partial^2 E_\alpha}{\partial z^2} \ll k_z \frac{\partial E_\alpha}{\partial z}, \tag{12}$$

and using Eq. (1) we have

$$ik_\alpha \frac{\partial E_\alpha}{\partial z} = \mu_o \frac{\partial^2}{\partial t^2}[P^{(3)}(\omega_\alpha, z, t)]e^{-i(k_\alpha - \omega_\alpha t)}. \tag{13}$$

In this derivation, the relationship between the linear susceptibility $\chi^{(1)}$ and the dielectric constant $\epsilon = (1 + \chi^{(1)})$ is employed, while the $P^{(2)}$ term is omitted since it vanishes in the class of centrosymmetric media, of which diamond is a member. This last point is justified below, as we now need to diverge slightly and examine the polarization source term in more detail.

2.2.1.1 Polarizations aspects

$P^{(3)}$ is expressed in component form as

$$P_i(\omega_3) = \chi_{ijkl}(\omega_3,\omega_0,\omega_1,\omega_2)E_j(\omega_0)E_k(\omega_1)E_l(\omega_2)e^{i(k_0 + k_1 + k_2)\cdot z}, \quad (14)$$

where 0,1,2,3 number the frequencies and i,j,k,l labels the orientation of the induced polarization, and the polarizations of the incident fields respectively. $\omega_3 = \omega_0 + \omega_1 + \omega_2$ is the frequency of the electric field produced by this polarization, in this case the CARS frequency. The susceptibilities are assumed to be homogenous. This notation follows that of Maker and Terhune[2,5,15,10], and has a factor ¼ absorbed into the definition of $\chi^{(3)}$.

With reference to Eq. (1), we note that $\chi^{(1)}$ is the linear susceptibility, related to the dielectric constant and therefore the refractive index; $\chi^{(2)}$ gives rise to other non-linear phenomena (such as second harmonic generation), but disappears in centrosymmetric media due to symmetry concerns[19,15,18,6]; and $\chi^{(3)}$ gives rise to coherent Raman phenomena and is non-zero in all media. It is the fact that CARS arises from the coupling of the third-order susceptibility with three electric fields, that makes it sensitive to different information not obtainable from linear scattering. The possibility of mixing three waves with distinct frequencies, polarizations, phases and magnitudes to produce a CARS signal, allows the frequency, polarization, phase and magnitude of the signal to provide more molecular information than in the linear Raman case. For example by choosing the polarizations of the incident electric fields appropriately, and measuring the polarization of the CARS signal, one may establish the components of $\chi^{(3)}$.

Being a fourth-rank tensor, $\chi^{(3)}$ has 81 components. This number is reduced, firstly since the 3 pairs (j,ω_0), (k,ω_1) and (l,ω_2) are invariant to permutation. By convention only the distinguishable terms are included in the summation, so a factor $6/n!$ is included to explicitly show the degeneracy[15,9,10,3,2,6]; n being the number of indistinguishable pairs so that $n!$ is the number of indistinguishable permutations. The number of components is further reduced by the medium's symmetry. The tensorial definition relating the transformation of a tensor T, of rank R, from one reference frame into another

$$I_3 = \frac{c}{2}\sqrt{\epsilon_3\epsilon_0}|E_3|^2$$
$$\therefore I_3 = \frac{9}{16}\frac{\omega_3^2}{n_1^2 n_2 n_3}\left(\frac{\mu_0}{\epsilon_0}\right)^2 |\chi_{CARS}|^2 I_1^2 I_2 L^2 \mathrm{sinc}^2\left(\frac{\Delta kL}{2}\right). \quad (18)$$

The CARS intensity therefore varies as the square of the ω_1 field, "pump" laser beam, and linearly with the ω_2 or "Stokes" beam. The terms pump and Stokes are used since referring to Fig. 1, we see that for a strong CARS signal, $\hbar\omega_1 - \hbar\omega_2$ must equal the energy level difference between the two energy states, necessitating that ω_2 be a (linear) Raman frequency shift below ω_1; thus ω_2 is the Stokes electric field and ω_1 can be considered to be the pump electric field. The CARS signal is forward propagating[5], and depends on the square of the interaction length L, rather than linearly as in the spontaneous Raman case[4]. Druet and Taran[21] also state that should the pump beam be Gaussian, the CARS beam will also be Gaussian.

The phase matching condition is also clear from Eq. (18), i.e.

$$k_3 = 2k_1 - k_2, \quad (19)$$

which follows from the requirement of maximising the sinc^2 function. This maximum is obtained when $\Delta k = 0$ (perfect phase matching), and is an important aspect of the CARS technique. The generation of a detectable signal hinges on how well this momentum conservation condition is met. This is especially true in condensed phases, since the sinc^2 function drops rapidly to zero from its peak in a distance given by

$$L_c = \frac{\pi}{\Delta k}, \quad (20)$$

the coherence length[10,9,11,15]. In gaseous media Δn, as a function of the laser frequencies is always small, so that with

$$\frac{k}{\omega} = \frac{n}{c}$$
$$\Rightarrow \Delta k \propto \Delta n, \quad (21)$$

the coherence length for the CARS signal from gases is large enough so that the sinc^2 factor

is always close to unity. Thus phase matching of the input lasers in easily achieved (if the beams are focused), and collinear[4,10,3] operation of these input beams is often sufficient to produce the CARS signal. The major problem with the collinear arrangement is the lack of control of spatial resolution[4] and the interaction region of the laser beams, as well as discrimination between the CARS signal, fluorescence, and the input laser beams. CARS signal contributions from the optical elements, e.g. lenses are also unavoidable[4].

Proper phase matching requires a two-dimensional geometry to be employed to ensure that the two input laser beams cross at the appropriate angle (Fig. 2), thus increasing the coherence length and allowing for efficient growth of the CARS signal. This is essential in media where the dispersion is appreciable, e.g. solids, and preferable to tight focusing of collinear beams[11,10], where each beam contains a range of wave vectors which selectively combine to fulfil Eq. (19), as this reduces the signal intensity. Tight focusing of collinear beams has the advantage that the phase matching condition is always met.

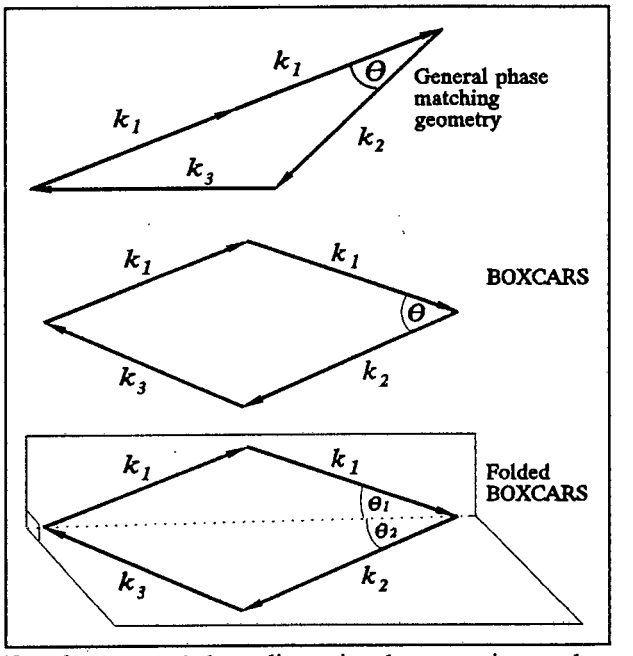

Fig. 2 Two- and three-dimensional geometries used to ensure phase-matching.

An adaptation of the general quadrilateral phase matching geometry was developed by Eckbreth[22,4] and involves three input wave vectors and a rhombic design known as BOXCARS. A three dimensional variation called folded BOXCARS[10,11] has also been developed. In folded BOXCARS, the ω_1 beams are contained in a plane orthogonal to that of ω_2 and ω_3.

Spatial separation of the CARS signal from the laser beams is achieved in all three geometries, while BOXCARS and folded BOXCARS permits small Raman shift to be isolated[5,11,4]. For large enough Raman shifts, dichroic filters are used to separate the CARS signal from the laser beams, but with small shifts this is not possible with these filters. The

BOXCARS geometries however, permit the small Raman shift to be substantially separated in space from the laser beams. BOXCARS also allows for greater spatial resolution[10,4,11,3] and control of the interaction region[22,4,3]. Proper phase-matching also has the advantage of suppressing superfluous CARS signal generation from any of the experimental components[11]. The geometric restriction imposed by phase matching proves to be one of the major constraints of the CARS technique.

Finally, note that $I_3 \propto |\chi_{CARS}|^2$. In establishing the form for χ_{CARS} through either quantum mechanics or the lattice mode interaction, it is apparent that the susceptibility is complex, and that it can also contain a non-resonant contribution from one- and two-photon electronic resonances. Thus the susceptibility can be written as

$$\chi_{CARS} = \chi' + i\chi'' + \chi_{NR}, \tag{22}$$

where the first two terms are the real and imaginary Raman contributions and the final term the non-resonant contribution. Since the norm of Eq. (22) is being used in I_3, interference between the three contributing terms occurs, altering the spectral lineshape (see further § 2.5). Much time and effort has been directed in particular towards reducing the effect of χ_{NR}, and many ingenious techniques have been formulated in this regard.

2.3 Lattice mode vibration derivation of χ_{CARS}

A semi-classical derivation for the form of $\chi^{(3)}$ is now presented, as this allows us to understand simply the essential features of the CARS process. However, since CARS is a resonance phenomenon this interpretation is not valid at resonance, and recourse to quantum mechanics is essential for a correct understanding of the process. The quantum mechanics is technically difficult since it involves third-order perturbation theory with damped states and will be presented in the next section, while the easier semi-classical interpretation is discussed below. This method to establish the form of χ_{CARS} is employed by Maeda *et al.*[11], Levenson *et al.*[10,7,8] and Nibler *et al.*[15] The scheme consists of a Raman-active molecular vibration excited by the two laser beams, followed by inelastic scattering off this vibration.

Bloembergen[18] uses an anharmonic oscillator model in his derivation. The linear induced polarization in the one dimensional case $P = \alpha(E_1 + E_2)$, gives rise to a potential energy

$$-\tfrac{1}{2}\alpha E^2, \tag{23}$$

which leads to a force

$$\frac{1}{2}\left[\frac{\partial\alpha}{\partial Q_\sigma}\right]_0 E^2, \tag{24}$$

driving a molecular vibration where Q_σ is the normal coordinate of mode σ, and α is assumed to vary with position. The complex electric fields result in sum and difference frequencies arising in Eq. (24), so that when the damped harmonic oscillator equation for the lattice vibration

$$m\ddot{Q}_\sigma + m\Gamma_\sigma\dot{Q}_\sigma + m\omega_\sigma^2 Q_\sigma = F \tag{25}$$

(where ω_σ is the normal frequency, in our case equal to the Raman shift ω_R) is solved, one obtains[11]

$$Q_\sigma = \frac{1}{8m\omega_\sigma}\left[\frac{\partial\alpha}{\partial Q_\sigma}\right]\frac{E_1E_2^*}{\delta - i\Gamma_\sigma}e^{i(\omega_\sigma - \delta)t} + c.c., \tag{26}$$

where $c.c.$ = complex conjugate, $\delta = \omega_R - (\omega_1 - \omega_2)$ is the detuning from Raman resonance, and m is the oscillator (dipole) mass. Levenson *et al.*[7] assume a linear approximation for the modulation of the polarization

$$\Delta\chi = N\sum_\sigma \alpha Q_\sigma, \tag{27}$$

and that the third-order polarization changes accordingly to give

$$\chi^{(3)}_{ijkl} = \frac{N}{6m}\sum_\sigma\left[\frac{\alpha_{ij,\delta}\alpha_{kl,\delta} + \alpha_{ik,\delta}\alpha_{lj,\delta}}{\omega_\sigma^2 - (\omega_1-\omega_2)^2 + i\Gamma_\sigma(\omega_1-\omega_2)}\right] + \chi_{NR}, \tag{28}$$

where again χ_{NR} (also a rank four tensor) is due to one-photon electronic absorptions and the corresponding two-photon absorptions have been ignored. Eq. (28) is a slightly modified form of the Levenson equation, altered to be consistent with our notation. Maeda *et al.* arrive

at

$$\chi^{(3)} = \frac{\chi_R}{\delta - i\Gamma_\sigma} + \chi_{NR}, \tag{29}$$

where

$$\chi_R = \frac{N}{2m\omega_\sigma}\left[\frac{\partial\alpha}{\partial Q_\sigma}\right]_0^2, \tag{30}$$

is the resonant component, and σ refers to the Raman-active $\omega_R = \omega_1 - \omega_2$ mode. Again in both Eqs. (28) and (29), χ_{NR} is essentially real if the electronic interactions are off resonance. Kleinmann[23,10] noted that provided the frequencies of the incident light were below that of the electronic transitions, the indices of the nonlinear susceptibility tensor can be permuted at will, separately from the arrangement of its frequency arguments. Kleinmann also states that this contribution to the measured optical signal will be flat with respect to frequency, thus the term background or non-resonant susceptibility. This condition is termed Kleinmann symmetry and was investigated in centrosymmetric media by Levenson and Bloembergen[8].

2.4 Quantum Mechanical form for χ_{CARS}

In this section we apply perturbation theory to the dipole matrix operator to obtain expressions for the various terms contributing to the non-linear susceptibility. We begin by expressing the polarization in terms of quantum mechanical operators. Classically it is defined to be the bulk dipole moment per unit volume, so that quantum mechanically we can write this as the ensemble average[15,5,6,18,11,10] of the dipole moment operator μ, i.e.

$$\langle P(r,t)\rangle = N\overline{\langle\psi|\mu|\psi\rangle} = N\,\mathrm{Trace}(\rho\mu) = \Sigma\rho_{gt}\mu_{tg}. \tag{31}$$

μ_{tg} is then the transition dipole moment matrix between eigenstates t and g, and $\rho = |\psi><\psi|$ is the density matrix operator described by

$$i\hbar\dot{\rho} = [H_0 + H_{int}, \rho] + i\hbar\Gamma\rho. \tag{32}$$

H_0 is the unperturbed Hamiltonian, and $H_{int} = -\mu\cdot E$ the interaction of the dipole with the applied field, i.e. the perturbation. The damping term Γ describes the rate at which the

perturbed system relaxes to equilibrium. It results in linewidth terms in the resonance denominators of the susceptibility expressions. Diagonal elements Γ_{gg} represent population relaxation rates due to spontaneous emission and inelastic collisions (T_1 processes) (see Levenson[10]), while off-diagonal terms $\Gamma_{gt} = \frac{1}{2}(\Gamma_{gg} + \Gamma_{tt}) + \Gamma_{gt}^{e}$ result from broadening of the two states plus an elastic collision (T_2 processes) dephasing contribution Γ_{gt}^{e} [5,6,10,11].

Perturbation theory then leads to

$$\begin{aligned} i\hbar\dot{\rho}^{(0)} &= [H_0,\ \rho^{(0)}] + i\hbar\Gamma\rho^{(0)} \\ i\hbar\dot{\rho}^{(1)} &= [H_0,\ \rho^{(1)}] + [H_{int},\ \rho^{(0)}] + i\hbar\Gamma\rho^{(1)} \\ i\hbar\dot{\rho}^{(n)} &= [H_0,\ \rho^{(n)}] + [H_{int},\ \rho^{(n-1)}] + i\hbar\Gamma\rho^{(n)}. \end{aligned} \tag{33}$$

Successive solutions of these equations leads to an expression for $\rho_{gt}^{(3)}$ in terms of the equilibrium densities ρ_{gg}^{0}, ρ_{tt}^{0}, etc. Combined with Eqs. (31), (1) and (14), these yield the general 48 expressions for the terms of $\chi^{(3)}$. These are acquired either purely algebraically, or through the application of double-sided Feynman diagrams, with the appropriate vertex rules. This graphical method, first proposed by Feynman, has been extended by Hewitt and is used by many authors[5,6,15,11,9,17].

Nibler and Pubanz[6] show that selecting the terms contributing only to the CARS susceptibility results in

$$\begin{aligned} \chi_{CARS} = \chi_{\epsilon\alpha\beta\gamma} = & \\ & \sum_{if} \frac{N}{8\hbar^3(\omega_{fi} - \omega_1 + \omega_2)} \sum_{j} \left[\frac{\mu_{fj}^{\beta}\mu_{ji}^{\epsilon}}{\omega_{ji} - \omega_3} + \frac{\mu_{fj}^{\epsilon}\mu_{ji}^{\beta}}{\omega_{jf}^{*} + \omega_3} \right] \\ & \times \sum_{k} \left[\rho_{ii}^{0} \left[\frac{\mu_{ik}^{\gamma}\mu_{kf}^{\alpha}}{\omega_{ki} + \omega_2} + \frac{\mu_{ik}^{\alpha}\mu_{kf}^{\gamma}}{\omega_{ki} - \omega_1} \right] - \rho_{ff}^{0} \left[\frac{\mu_{ik}^{\gamma}\mu_{kf}^{\alpha}}{\omega_{kf}^{*} + \omega_1} + \frac{\mu_{ik}^{\alpha}\mu_{kf}^{\gamma}}{\omega_{kf}^{*} - \omega_2} \right] \right] \\ & + \{\alpha \leftrightarrow \beta\}, \end{aligned} \tag{34}$$

where $\omega_{lm} = (\omega_l - \omega_m) - i\Gamma_{lm}$. Eq. (34) contains one-photon resonance Raman polarizability elements, but not two-photon resonances. Away from electronic contributions, this becomes[6,11,10,3]

$$\chi_{CARS} = \sum_{ij} \frac{N_i - N_f}{8\hbar(\omega_{fi} - \omega_1 + \omega_2)}(\alpha_{\epsilon\alpha}\alpha_{\beta\gamma} + \alpha_{\epsilon\beta}\alpha_{\alpha\gamma}) + \chi_{NR}. \tag{35}$$

N is the population density and α the spontaneous Raman polarizability $\chi^{(1)}$. For spontaneous Raman Stokes scattering, the scattering cross-section for light of frequency ω_1 is

$$\left[\frac{d\sigma_{fi}}{d\Omega}\right]_{\beta\epsilon} = \left[\frac{\omega_2}{c}\right]^4 |\alpha_{\beta\epsilon}|^2, \tag{36}$$

implying that the conventional Raman scattering cross-section is obtainable from CARS, since from Eqs. (35) & (36) both are proportional to α^2. CARS therefore provides basically the same transition frequency and cross-section information as in spontaneous Raman scattering. χ_{NR} is essentially real so that $i\Gamma_{fi}$ (HWHM) is the primary imaginary term. As alluded to at the beginning of this chapter, we now see that if $\omega_1 - \omega_2 = \omega_R$, where $\omega_R = \omega_{fi}$ (the energy difference between the initial and final energy levels), the CARS signal will be resonantly enhanced, and much stronger than if it were off resonance.

2.5 Effect of non-resonant susceptibility

Referring to Eqs. (18), (22) & (29) and the previous discussions, it can be shown that[11,3]

$$I_3 \propto |\chi_{CARS}|^2 = \chi_{NR}^2 + \frac{2\chi_{NR}\chi_R}{\delta^2 + \Gamma^2}\delta + \frac{\chi_R^2}{\delta^2 + \Gamma^2}, \tag{37}$$

where the identifications

$$\chi' = \chi_{NR} + \frac{\chi_R\delta}{\delta^2 + \Gamma^2}, \tag{38}$$

and

$$\chi'' = \frac{\chi_R\Gamma}{\delta^2 + \Gamma^2}, \tag{39}$$

have been made. The contributions of these three terms are shown in Fig. 3. From Eq. (37), the non-resonant term bestows a constant background to the signal spectrum, while the

second term tends to deform the Lorentzian (third term) lineshape[11,5,3]. Elimination of χ_{NR} would leave only the Lorentzian lineshape, so reduction of this contribution is consequently essential. This is especially true for weak signals which would be undetectable with a background contribution present. This elimination or reduction can be achieved through proper choice of polarizations[4,5] of the laser light, utilising the symmetry properties of the medium, to separate the CARS and non-resonant signal components. Unfortunately this is only possible with highly symmetrical media such as liquids or gases. This is most easily seen in the isotropic case[5,15,9] where, under the assumption of Kleinmann symmetry, the non-resonant contribution is eliminated when the lasers are polarized at 60° relative to each other.

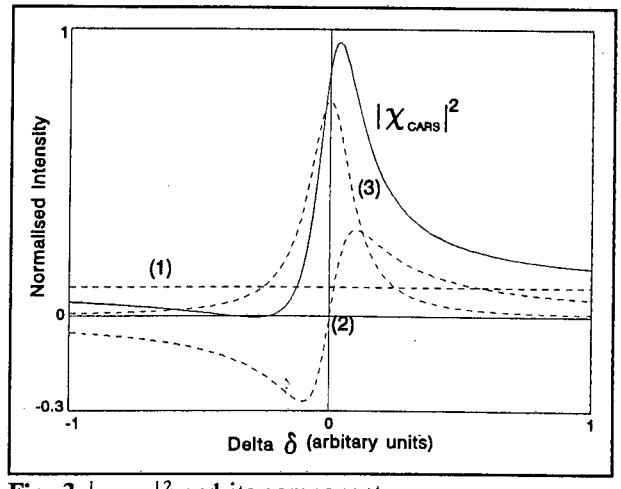

Fig. 3 $|\chi_{CARS}|^2$ and its components.

Some authors[15,7,8,11] use a lineshape analysis involving the minimum, maximum, middle intensity and corresponding frequency values of $|\chi_{CARS}|^2$ to calculate exact Raman resonance χ_R, and the damping constant or CARS lifetime Γ. This form of analysis is used when it is not possible to eliminate the χ_{NR} contribution to the measured CARS signal, and numerical curve-fitting is difficult.

Chapter 3

Apparatus and experimental setup

In this chapter, we discuss the experimental equipment used during this study, as well as the various experimental setups employed. Aspects of diamond that influenced the equipment and these setups are also examined.

3.1 Description of Equipment

3.1.1 Lasers

The UCT Laser Laboratory possesses a special CARS laser system manufactured by SOPRA of France. This comprises two lasers constructed on a single table with components in an open configuration, i.e. all laser components are uncovered and easily accessible. The first laser is a pulsed, single longitudinal mode (SLM), frequency-doubled, passively Q-switched Nd:YAG producing green light at wavelength $\lambda_1 = 532$ nm. This is used to pump transversely a broadband dye laser at a longer wavelength, which is determined by the particular experiment being performed and therefore the type of dye being used. The energy of the laser pulses ranges from 15 - 200 mJ for the Nd:YAG laser, and 5 - 10 mJ for the dye. A schematic of the laser system is shown in Fig. 4.

Ideally, for studying the rather narrow CARS resonance in diamond, both lasers used (pump and Stokes) should be narrowband light sources. This would exploit all the input energy optimally, resulting in high resolution, high intensity spectra with minimal line broadening. No narrowband laser source at the appropriate Stokes wavelength for this work with diamond was available to us, so this idea was abandoned. However, a narrowband Stokes source could possibly be generated through the emission of Stimulated Raman Scattering (SRS) from a diamond crystal, and this could be used with the Nd:YAG emission to produce the CARS

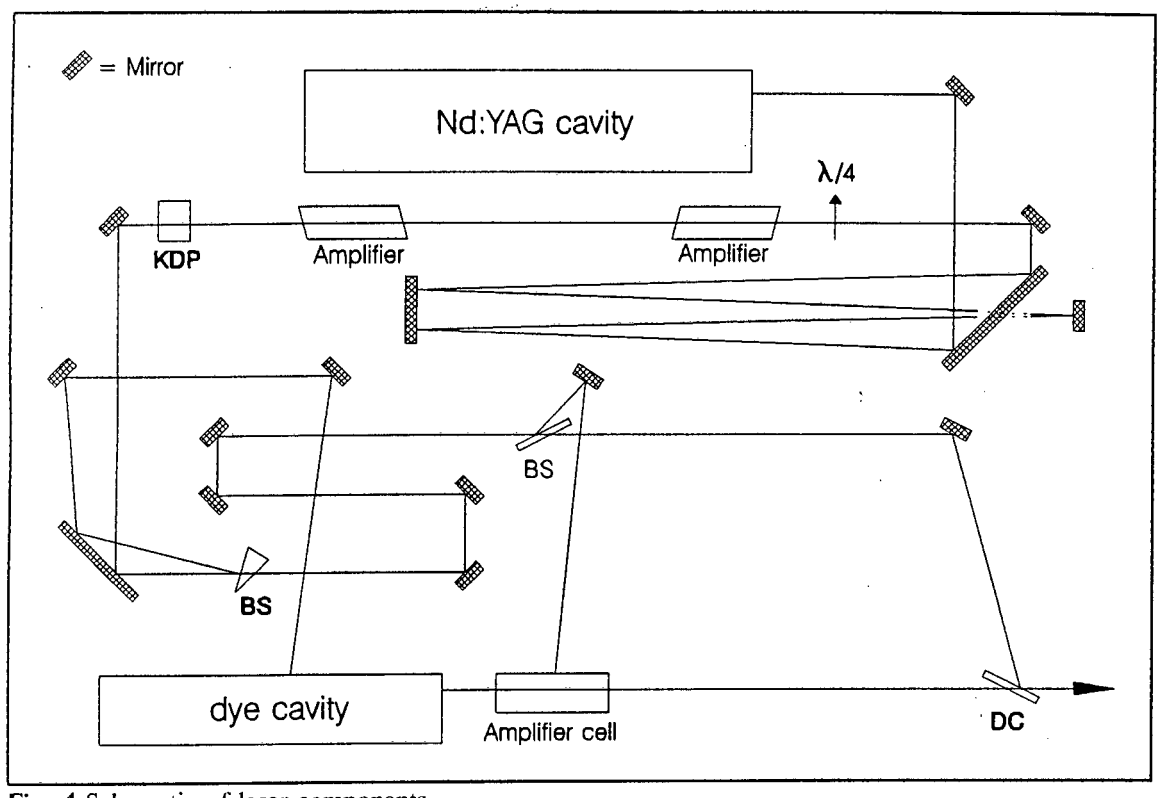

Fig. 4 Schematic of laser components.

signal. This system would retain the above mentioned advantages of narrowband sources, in addition to being completely solid state. However, an attempt to induce SRS in diamond failed, and this attempt together with reasons for the failure, will be discussed in detail in the next chapter. We thus had to default to using the broadband dye laser source since this was available, and since the cost of acquiring or building a narrowband laser source was not justifiable within the scope of this work. The combination of a broadband Stokes source and narrowband pump source has the advantage, especially for complex spectra, that the entire CARS spectrum is generated simultaneously.

A 1064 nm infra-red (IR) beam is obtained by the pulsed energising of a Nd:YAG rod, through the discharge of the neighbouring krypton flash lamps. This oscillator resides inside a folded cavity encompassing a concave mirror of radius 1 m at one end, and a long (100 mm) Fabry Perot (FP) étalon of reflectance 4% at the other. Another short (5 mm) FP étalon of reflectance 65% is also housed in this cavity. The SLM operation of the laser is accomplished by the combined effect of both étalons. The cavity is folded to allow the étalons to be located on a single stand, so that both étalons are thermostatted together and temperature control of the étalons is easier.

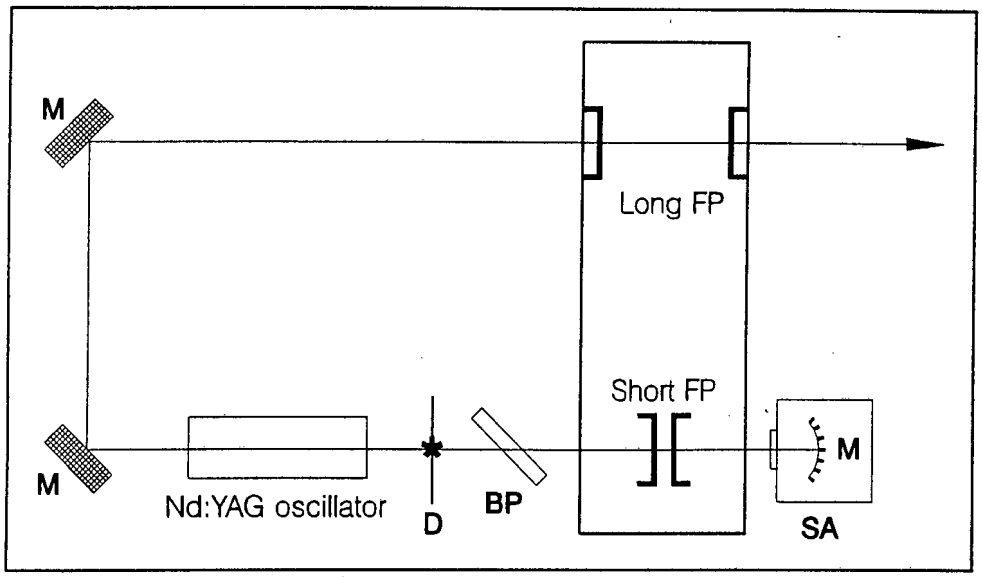

Fig. 5 Components of the Nd:YAG laser cavity.

A saturable absorber cell located at the concave mirror and containing a solution of bis(4-dimethylaminodithiobenzyl nickel) (BDN) in dichloroethane (DE) is responsible for the passive Q-switching of the cavity. Increasing the BDN concentration shortens the pulse length. The pulse length is adjusted to be in the range 15 - 20 ns, as shorter pulses would damage the concave mirror while longer ones decrease the frequency-doubling efficiency of the KDP crystal. A pulse length $\simeq$ 17 ns was used during this study. A polarizer inclined at the Brewster angle (57°) produces a horizontal polarization on the IR radiation by reflecting out of the cavity only vertically polarized light, thus spoiling the gain of the cavity and favouring horizontally polarized light. Finally a diaphragm with circular aperture of diameter 2 mm which suppresses all but the lowest order transverse mode (TEM_{00}), is situated between the Nd:YAG rod and the polarizer.

The IR beam leaves the cavity and passes through a two-stage amplification system before being frequency-doubled by a type 2 KDP (potassium dihydrogen phospate) crystal. This is most efficient in frequency conversion when the input radiation is circularly polarized. The $\lambda/4$ plate before the amplifiers performs this task. The amplifiers are again 7 mm diameter YAG rods, so to maximize the amplification of the IR beam, the 2 mm diameter beam must be expanded to $\approx$ 7 mm in order to fill the amplifiers completely. This increase in diameter is accomplished by allowing the beam to expand under its own diffraction, before being

amplified. Multiple reflections across a folded path length of 6 m ensures sufficient diffraction to expand the beam to the desired 7 mm diameter.

The frequency-doubled (green) beam is then split off at two stages by beamsplitters (BS) and used to pump and amplify the dye laser. The dye laser has both oscillator and amplifier cells through which a dye solution flows. These are pumped transversely by the Nd:YAG beam, and for maximum emission from the dye, both the dye laser beam and the green beam must have the same polarizations. This is only possible if both are vertically polarized, and the KDP crystal is aligned so that it emits vertically polarized light.

The dye solution used in the dye laser is stored in flasks attached to an electric pump and plastic tubing. The flasks are flushed clean with the solvent when the dye is being changed, and a solution of the dye in ethanol is then added to the flasks. Increasing the concentration of the solution increases the dye laser wavelength and this allows for selection of the appropriate wavelength or wavelength range.

The dye laser operates broadband over a range of approximately 10 nm, this varying with the particular dye. Too high a dye concentration however means that the pumping Nd:YAG beam will be absorbed in a shorter distance in the dye cell, producing non-circular dye beam profiles. Thus the dye concentration needs to be adjusted for both dye laser wavelength and beam quality. Crescents and incomplete discs profiles with diameters of 8 mm, have been observed. Interference rings due to the dye cavity are also visible in the profile. The Nd:YAG beam profile is elliptical in shape with dimensions 6 mm horizontally and 4.5 mm vertically. Thus the lasers' beam profiles are not Gaussian or plane waves, but a more complex combination of these.

Finally the path of the green laser beam is folded to ensure that it emerges in temporal coincidence with the dye laser beam.

3.1.2 Operation of the Étalons

It is important to examine the detailed workings of the étalons contained in the Nd:YAG cavity, as these are very effective in producing single longitudinal mode stability of the Nd:YAG beam. This stability unfortunately affected an attempt at Stimulated Raman Scattering (SRS) production in diamond, so discussion of how the laser is designed to passively maintain a single longitudinal mode is needed.

The laser cavity is physically 1 m long, but due to refractive components contained within, notably the 115 mm long oscillator Nd:YAG rod of refractive index 1.818, it has an optical path length of 1.1 m. Longitudinal modes of frequency

$$\nu_{cav} = \frac{mc}{2L}, \tag{40}$$

will be sustained by the cavity, where m is the mode number, L the optical cavity length and c the speed of light. More importantly the mode separation will be

$$\Delta\nu_{cav} = \frac{c}{2L}, \tag{41}$$

where the subscript *cav* denotes the cavity. The étalons can be described by multiple beam interference[24] with their relative transmissions given by

$$\frac{I_t}{I_i} = \left[1 - \frac{A}{(1 - R)}\right]^2 \frac{1}{[1 + F\sin^2(\delta/2)]}, \tag{42}$$

where R is the reflectance, A the absorptance (negligible in our case), and the ratio

$$F = \frac{4R}{(1 - R)^2}, \tag{43}$$

is related to the finesse. The phase difference δ between successive interfering light rays is defined as

$$\delta = \frac{4\pi n}{\lambda} d\cos\theta_t + 2\phi, \tag{44}$$

where n is the étalon refractive index, d its length, θ_t the angle at which the light leaves the étalon and ϕ an additional phase shift introduced by reflections. The étalon reflectance is then just 1 - Eq. (42). Within the laser cavity, the radiation is nearly normal to the étalons so that we may let $\theta_t = 0$. Now from Eq. (42), the transmitted light will be a maximum when $\delta = 2\pi m$, and Eq. (44) then shows that the difference in frequency between the transmitted frequencies, often referred to as the free spectral range, is

$$\Delta\nu_{ét} = \frac{c}{2nd}. \tag{45}$$

Eq. (45) obviously also hold true for the reflected light. The number of cavity modes in one transmission or reflection cycle of a single étalon is then simply

$$\frac{\Delta\nu_{ét}}{\Delta\nu_{cav}} = \frac{L}{nd}. \tag{46}$$

The Nd:YAG gain curve has a bandwidth on the order of 30 GHz, thus with $\Delta\nu_{cav} \approx 140$ MHz, there will be ≈ 220 potential cavity modes. The long étalon is used in reflection and its effect, from Eq. (46), is to overlap with only 29 of these modes. The short étalon is used in transmission (positioned so that reflected IR light leaves the cavity), and from Eq. (46) again, has only 1 mode in common with the laser cavity. Its high reflectance modulates the cavity modes (Eq. (42)), so that only 9 have a transmission of more than 90%. The gain curve and modulation of the cavity modes are graphically illustrated in Fig. 6. The overall modulation, the product of the curves in Fig. 6, is depicted in Fig. 7.

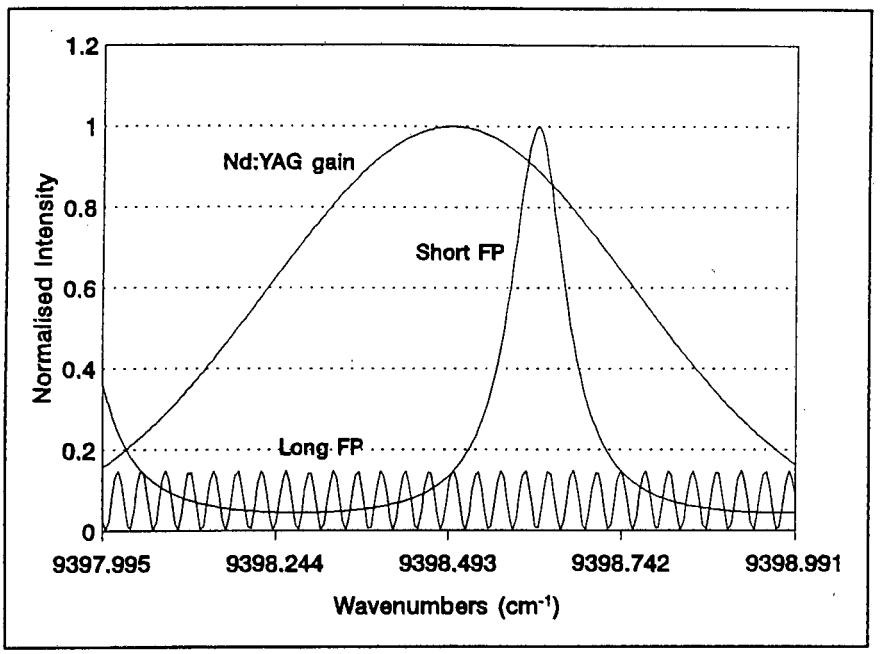

Fig. 6 Individual modulations of the Nd:YAG IR radiation due to the short and long Fabry Perot étalons.

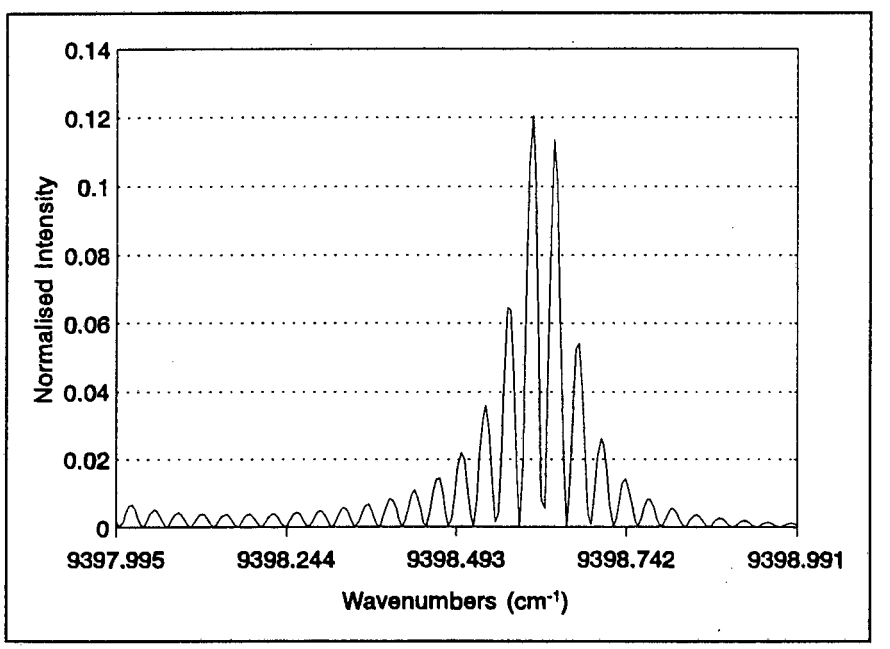

Fig. 7 Overall transmission of Nd:YAG IR radiation due to superposition of cavity and FP étalon modulations.

This is a typical condition for the cavity to be in, and single longitudinal mode operation is assured since the mode with highest intensity (only one exists) will go through threshold first and be amplified by the cavity gain. The other modes will then not reach threshold at all, and all the energy stored in the Nd^{3+} population inversion will be used in amplification of the solitary mode. In practice dual-mode shots are occasionally observed, this being due to the laser table heating up and the cavity length L expanding marginally. ν_{cav} then changes, as does $\Delta\nu_{cav}$ and the effect of the étalon modulate is to produce two modes with equal (or very nearly equal) intensities. Both reach threshold (nearly) simultaneously and a dual-mode shot is amplified. Three-mode beating is very unlikely, and has not been observed during this research.

3.1.3 Spectrometer

The spectrometer used in the Laser Laboratory is a SOPRA CARS CS02 0.75 m spectrometer with a 60 mm diameter 2100 lines per mm holographic grating. A 1024 channel EG&G Princeton Applied Research Corporation (PARC) Optical Multi-channel Analyser (OMA) is used for detection. An appropriate detector controller provides the high voltage supply and interface to the OMA. This controller also digitised the OMA response for data processing by computer. Thus the diode response is presented as 1024 consecutive pixels.

The OMA detector is an intensified photo-diode array, each diode being 25 μm wide. The dispersion of the spectrometer/OMA combination at the CARS wavelength for diamond (see § 3.2.1) is 0.259(6) cm^{-1}/pixel. The corresponding grating resolution is $\simeq 1/6.26\ cm^{-1}$, equivalent to 0.62 of a pixel. When the f-numbers of the spectrometer and the input light (in this case the CARS beam) are matched, the beam size at the entrance slit is $\approx$ 10 microns translating to an image size on the OMA detector $\approx$ 20 microns. This is again less than the breadth of one diode. The largest source of spectrometer/OMA error is the cross-talk from the OMA diodes due to the electronic intensification process and amounts to two or three pixels. The detector has been found to obey Poisson statistics i.e. for N shots of equal intensity, the error is $\sqrt{N}$.

3.2 Experimental setup

The experimental setups used are strongly influenced by particular properties of the sample, especially the exceptionally high refractive index of diamond. A discussion of these properties of diamond is therefore needed before proceeding, and is now presented.

3.2.1 Diamond

Diamond consists of carbon atoms covalently bonded in a cubic crystal structure with space group $Fd3m$[25], so that its point group is $m3m$[26]. The Bravais lattice is face-centred cubic with a basis of two carbon atoms at coordinates (0,0,0) and (¼,¼,¼). The coordination number is 4, these nearest neighbours arranged at the corners of a regular tetrahedron[25]. The tetrahedral angle is 109° 28′. Another description of this arrangement is that two face-centred cubic lattices with single carbon atoms at each lattice point are combined, or rather intermeshed and their origins displaced in a direction [¼,¼,¼]. This structure is sometimes called the diamond unit cell.

Using this crystal symmetry information with regard to the susceptibility structure and remembering the effect of CARS on this symmetry (described in Chapter 1), it can be deduced that there are 3 independent cubic susceptibility components[20],

χ_{ijji},
χ_{ijij} and
χ_{iiii},

with obvious degeneracies of 6, 6 and 3 respectively. However from group theoretical considerations it can be shown[27] that the derived linear susceptibility $\alpha_{ij,k}$ for this space group is non-zero and triply degenerate only for $i \neq j \neq k$. This implies that only one Raman-active mode exists for diamond and that $\chi_{iiii} = 0$, from Eq. (35) and Eq. (36).

The diamond crystal is clear and transparent to the eye when polished, while being an extremely hard substance. Three polished type IA diamond crystals cut along the (110) crystal plane, were kindly provided by De Beers Industrial Diamond (Pty.) Limited for this

work. Their useable dimensions were 5 mm × 2.5 mm × 1 mm, 5 mm × 4.5 mm × 1 mm and 5 mm × 4 mm × 1.5 mm, with two opposing faces being polished. These faces were nearly parallel, with this lack of perfect parallelism not being a hindrance experimentally. The crystals were used interchangeably in the experiments, these often repeated with a different crystal.

The Raman shift ν_R for diamond is 1332 cm^{-1} [7,28,29,30], this being known from spontaneous Raman spectroscopy. This information allows the calculation of the Stokes and CARS wavelengths from Eqs. (3) and (4), given the pump Nd:YAG laser wavelength of $\lambda_1 = 532$ nm. The Stokes wavelength is $\lambda_2 = 572.6$ nm (yellow-orange) while the CARS wavelength is expected at $\lambda_3 = 496.8$ nm (in the blue of the visible spectrum).

The phase matching condition Eq. (19), as shown in the BOXCARS geometry Fig. 2, required the calculation of the pump and Stokes crossing angle θ. From Fig. 2 and elementary mathematics this is

$$\begin{aligned} k_3^2 &= (2k_1)^2 + k_2^2 - 2(2k_1)k_2\cos\theta \\ \therefore\ \theta &= \arccos\left(\frac{k_3^2 - (2k_1)^2 - k_2^2}{-2(2k_1)k_2}\right), \end{aligned} \tag{47}$$

where

$$k_i = \frac{n_i\omega_i}{c} = \frac{2\pi n_i}{\lambda_i}. \tag{48}$$

Values for the dispersive refractive index for diamond were obtained[31] and used to fit the Cauchy equation[24]

$$n = A + \frac{B}{\lambda^2} + \frac{C}{\lambda^4} + \ldots, \tag{49}$$

to second order in λ only, and our required n_1, n_2 & n_3 (equal to 2.4261, 2.4197, & 2.4329 respectively) were interpolated from this. θ was found to be 1.48°. However, we have to remember that this is the crossing angle for the two beams inside the diamond crystal, which must not naively be thought to be the same as outside, i.e. in air. This is due to diamond's

high refractive index of 2.4 which implies that the crossing angle in air ϕ (see Fig. 8) will be different to θ.

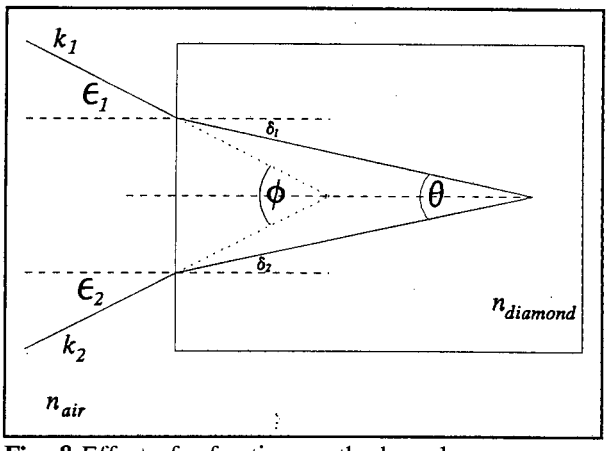

Fig. 8 Effect of refraction on the laser beams.

The geometry of Fig. 8 together with Snell's law give

$$\begin{aligned} \sin\epsilon_1 &= n_1\sin\delta_1 \\ \sin\epsilon_2 &= n_2\sin\delta_2 = n_2\sin(\theta - \delta_1), \end{aligned} \tag{50}$$

so that the outside crossing angle is

$$\begin{aligned} \phi &= \epsilon_1 + \epsilon_2 \\ &= \arcsin[n_1\sin\delta_1] + \arcsin[n_2\sin(\theta - \delta_1)]. \end{aligned} \tag{51}$$

This allows us to select any reasonable incident pump beam angle, δ_1. A spreadsheet was constructed with all possible δ_1's, the corresponding ϕ's and focal length of the converging lens to be used, given the Nd:YAG beam diameter. This allowed us to select the appropriate lenses to use from our stock, and to design the experimental setup accordingly. Note that with ϕ fixed, rotation of the crystal changes the δ's and therefore θ. This allows the intensity dependence of the phase matching factor $\text{sinc}^2(\Delta kL/2)$, to be studied by rotation of the diamond crystal.

3.2.2 Laser dye

With this Stokes wavelength in mind, the best dye to use in the dye laser turned out to be Rhodamine 6G (Rh 6G), since it peaks at 568 nm with a bandwidth of 40 nm from 552 nm to 592 nm, when dissolved at a concentration of 0.14 g/l in methanol[32]. A solution of ethanol (EtOh) and Lambda Physik LC 5900 MW 479.02 Rh 6G dye was prepared for the dye laser. The peak dye laser wavelength was adjusted as described above with an eventual concentration of 0.179 g/l in the oscillator circuit and 0.0314 g/l in the amplifier circuit. When the dye solution was changed for the second round of experiments, the concentrations turned out to be 0.216 g/l and 0.0361 g/l respectively.

3.2.3 Dichroic mixing plate and experimental setups

A key component in the CARS system is the dichroic mixing plate (filter) for combining pump and Stokes pulses. We preformed some preliminary experiments with the dichroic mixing plate supplied as standard on the SOPRA CARS laser table. This mixing plate was optimised for N_2 thermometry, with a centre wavelength λ_0 = 570 nm. It is a long wave pass filter which transmits the longer 607 nm dye radiation used for the nitrogen studies, and reflects the Nd:YAG beam. We established that the transmission of the 572.6 nm Rhodamine 6G dye radiation being used for this diamond CARS work, was too low. At shorter wavelengths, the transmission decreases rapidly. A dichroic mixing plate with λ_0 = 550 nm and optimised for the 572.6 nm Stokes transmission was then procured. This had to be manufactured being a non-standard optical component, and was not immediately available. In order not to lose valuable research time while waiting for this component, several experimental designs were used. Two types of detectors were also used, so that a total of 6 experimental variations were attempted, the complexity of each dictated by the particular CARS feature being studied. The phase matching condition in particular, required careful experimental setups in order to maximise the CARS signal. These variations will first be described below together with their pros and cons, and the experiments performed using these in the following chapter.

3.2.3.1 Experimental Setup 1

Fig. 9 shows the first experimental setup attempted. The green Nd:YAG and yellow dye beams leave the laser table parallel, through the use of a dichroic mixing plate (DC), and separated by ~ 10 mm, achieved by rotation of a translation plate (TP).

They are then reflected by a prism (P) into a 150 mm convex lens (L), and focused onto the sample (S) which is positioned by a goniometer. This instrument allows for six degrees of freedom; three translations and three rotations. This was important in selecting the correct internal crossing angles of the laser beams, as indicated in Fig. 8. A second 150 mm collecting lens ensures parallel propagation of the beams which then impinge onto a 500 nm

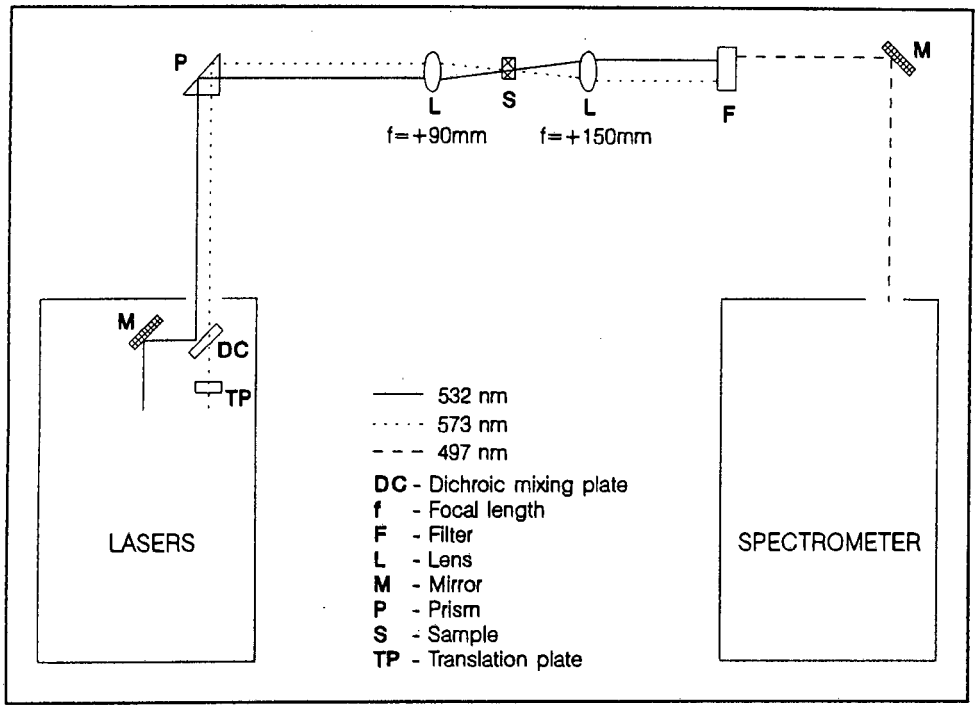

Fig. 9 Experimental Setup 1.

short-wavelength pass filter. The input laser beams are reflected, and the CARS signal (when present) transmitted, to be reflected into the spectrometer. The OMA is controlled by an EG&G PARC Detector Interface Model 1461, while an Elteknix 5502 20 MHz oscilloscope displays the spectrum, and a computer (PC) performs the shot triggering, electronic detection and storage.

This setup allows for the phase matching angle to be selected as unambiguously as possible, i.e. with Δk as nearly as possible equal to zero. After much adjustment of the various parameters available to us, viz. laser power, laser beams polarizations, placement of the sample in the beams path, and most importantly the crossing angle of the laser beams, we failed to detect the hoped for CARS radiation, other than for very rare flashes of collimated blue light.

Three points contributed to this failure:

(1) The standard $\lambda_0 = 570$ nm dichroic mixing plate was not suited for the dye wavelength, with more than 60% of the yellow light being reflected. The addition of an interference filter into the dye laser cavity to shorten the

bandwidth of the dye laser improved matters, but failed to solve the problem. This prompted the purchase of a custom built dichroic filter, reflecting 90% of the pump beam while transmitting an identical percentage of the Stokes beam at 45° incidence.

(2) The tight focusing of the laser beams by the first lens results in too high an intensity at the focal point ($\sim 1.3\times10^{11}$ W/cm^2), causing damage to the crystals by burning holes on the surface. The sample crystal thus had to be constantly moved to enable the laser beams to penetrate an undamaged area, only to be damaged further.

(3) The phase matching condition guarantees that the CARS beam should appear deviated from both the laser beams. This meant the CARS signal had to be detected visually, before it could be directed into the spectrometer. In hindsight it is likely that this experimental setup worked, but produced too weak a CARS signal to be detected by the eye. We did try to align the beam into the spectrometer, which at best of times is a very delicate operation, but since we could not see any signal, and because of the long distance to the spectrometer grating through a slit (3 m), we had a very small chance of succeeding.

Accordingly we abandoned this setup, and redesigned our experiment to account for the first two obstacles.

3.2.3.2 Experimental Setup 2

The modified experimental setup is shown in Fig. 10. The dichroic mixing plate was removed and a mirror employed to deviate the pump beam out of the laser table, while the dye beam was left undisturbed. The beams are crossed before the second mirror and 1 m from the 150 mm focusing lens. They therefore cross 170 mm from the lens, 20 mm from the focusing plane.

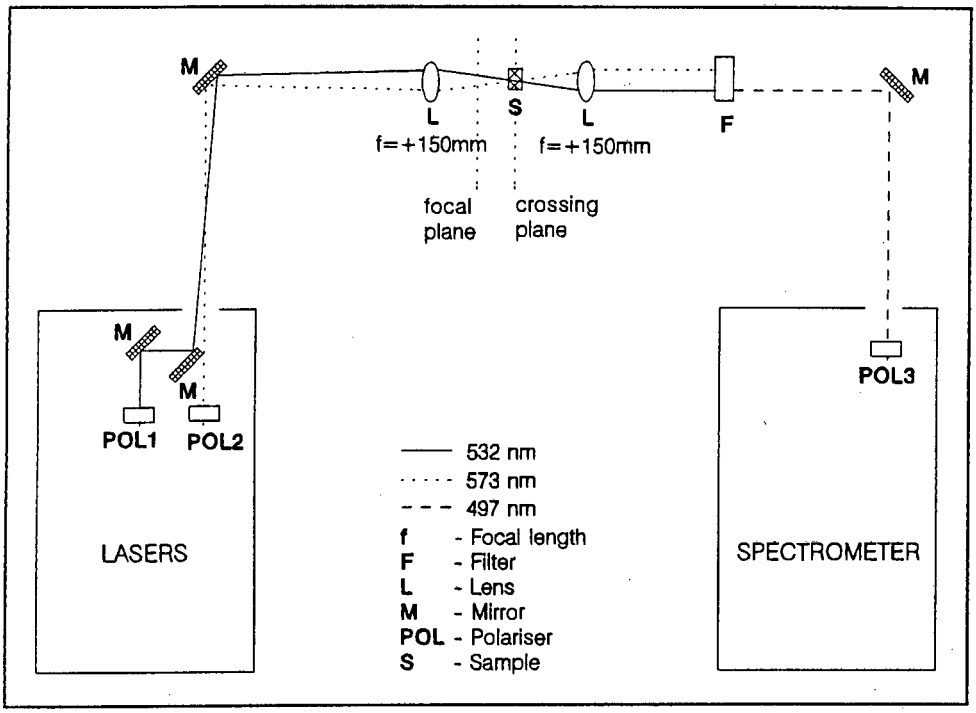

Fig. 10 Experimental Setup 2.

The sample is placed at this crossing (interaction) point, and a second collecting lens (also 150 mm) prevents further deviation of the laser and CARS beams. The 500 nm short-wavelength pass filter then reflects the input laser beams, and a mirror reflects the CARS signal into the SOPRA CARS CS02 spectrometer and attached OMA. The detection and storage apparatus was the same as used in Experimental Setup 1. The polarizing components POL1 and POL2 were rotatable and fixed $\lambda/2$ plates respectively, and POL3 was a Glan-Thompson polarizer. These were optionally included in the beam paths, depending on the nature of the experiment.

This configuration eliminates the need for a dichroic mixing plate, while utilising lower intensities ($\sim$ 19 MW/cm^2) and a larger spread of $\boldsymbol{k}$ vectors at the interaction point. These points mean that less of the dye beam-energy is lost, the crystals are not damaged and the probability of Eq. (19) being satisfied is significantly increased. However the spread of $\boldsymbol{k}$ vectors implies that $\Delta\boldsymbol{k} = 0$ is satisfied by a set of $\boldsymbol{k}_1$ and $\boldsymbol{k}_2$ vectors, so that an accurate investigation of the CARS intensity on sinc^2 could not be accomplished.

3.2.3.3 Experimental Setup 3

With the arrival of a dichroic mixing plate with λ_0 = 550 nm, optimised for beams at 532 and 573 nm, we wished to study the sinc^2 intensity dependence, so attempted the unfocused collinear arrangement shown in Fig. 11.

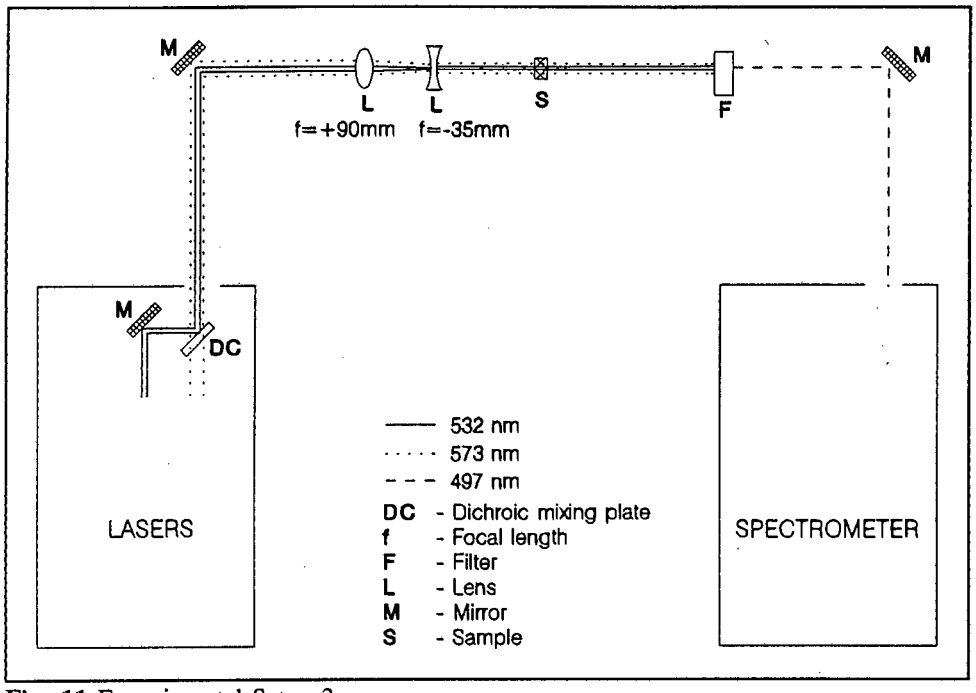

Fig. 11 Experimental Setup 3.

The schematic indicates the extent of the laser beams' waists, and not a typical ray as was previously the case. The dichroic mixing plate replaces the mirror, and the beams leave the laser table collinear. They are reflected onto the optics stand where their diameters are reduced by a Galilean telescope (a convex lens followed an appropriate distance by a concave lens), to increase the beams intensities. The beams enter the sample which can now be rotated to select the crossing angle unambiguously (Fig. 12), since $\boldsymbol{k}_1$ and $\boldsymbol{k}_2$ are now unique. As before the short-wavelength pass filter rejects the laser radiation, and the potential CARS signal is diverted into the spectrometer.

However, calculations of the required rotation of the sample to select the correct phase matching angle revealed that this setup would not produce a CARS signal at all. The crossing

angle is merely the difference in angles of refraction $|\delta_1 - \delta_2|$ for the two input beams, and this difference is at most 0.07° ($\ll$ 1.48°) due to the refractive indices n_1 and n_2 being too similar. This simple, elegant geometry consequently had to give way to an unavoidable complexity in order to test the CARS intensity sinc² dependence.

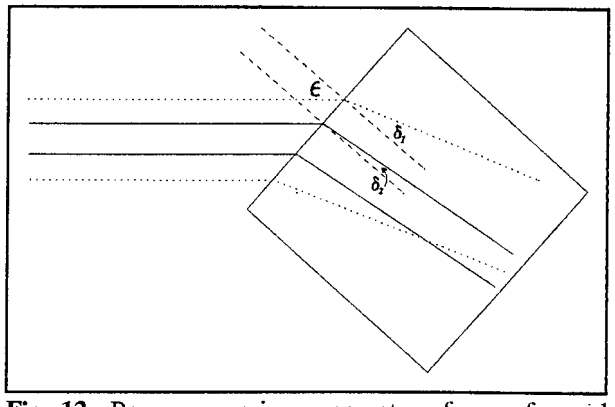

Fig. 12 Beams crossing geometry for unfocused collinear beams.

3.2.3.4 Experimental Setup 4

Fig. 13 is a schematic of the setup that enabled a proper investigation of the intensity sinc² dependence. The lasers' beams rays are indicated. The optional polarization components POL1 & POL2 were used in certain of the experiments performed with this setup, with POL1 again a rotatable λ/2 plate and POL2 begin either a fixed λ/2 plate or a Glan-Thompson polarizer.

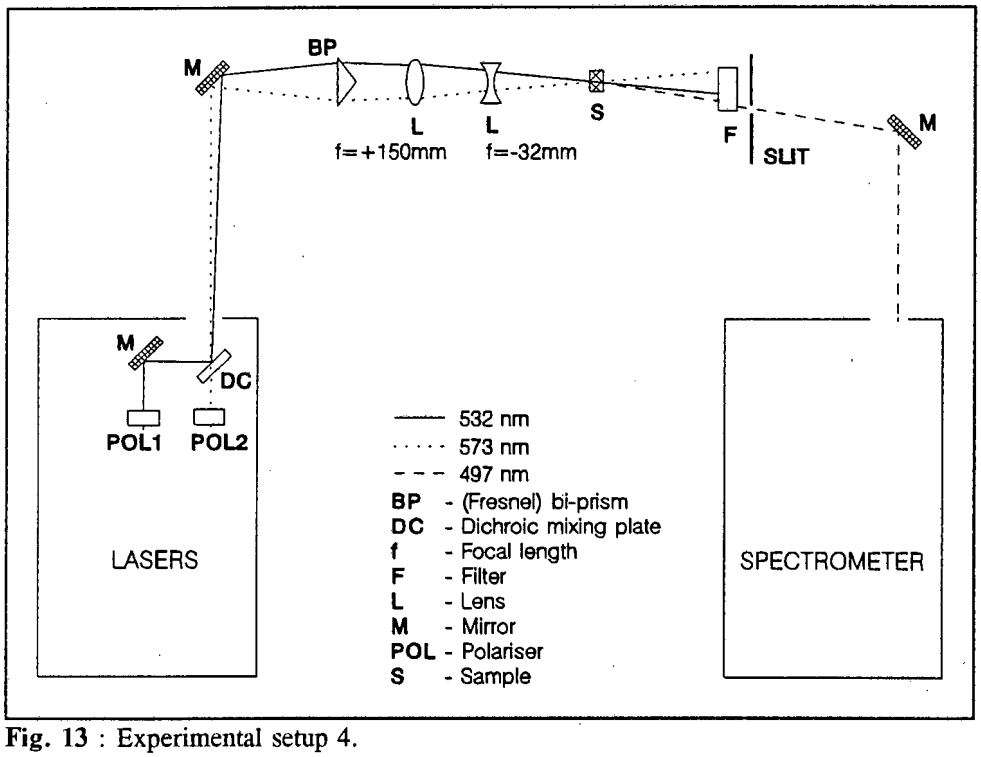

Fig. 13 : Experimental setup 4.

The appropriate dichroic filter is used to separate the green and yellow beams as they leave the laser table. These are deviated by a mirror (M) onto the optics bench where they pass through a Fresnel bi-prism (BP) to converge the rays. A reversed Galilean telescope comprising a 150 mm focal length converging lens and a −32 mm focal length diverging lens then reduces the beam waists. The beams cross at an angle obtained from the calculations mentioned earlier (§ 3.2.1), and the sample rotated within the beam crossing region to select the internal crossing angle ϕ.

The 500 nm short-wavelength pass filter reflects the laser beams and the CARS signal passes through a slit, which also serves to reduce strong scattered green and yellow light, such as that reflected from the laboratory walls. Note that the slit could have been used on its own to isolate the CARS signal due to the phase matching criterion, but the angular deviation of the CARS signal from the exceptionally bright green beam is small and to see the signal visually is impossible without the filter. The CARS signal is reflected into the spectrometer, which is the same as used in Experimental Setup 2, as is the associated detection and control equipment.

The beams crossing angle θ was found to be $\simeq 4.2 \pm 0.2°$, by removing all components after the diverging lens and measuring the beams' separation 2.1 m from their crossing point. The divergence of the beams at their crossing point was also established by measurement of their spot sizes (waists) at the crossing point and at this 2.1 m position.

To a first approximation the laser beams can be treated as being Gaussian at the crossing point, where they assume their minimum diameter. The Gaussian beam waist at a distance z from the minimum waist w_0 is given by

$$w(z) = w_0 \left[1 + \left(\frac{z}{z_r} \right)^2 \right]^{\frac{1}{2}}, \tag{52}$$

where the Rayleigh length z_r is

$$z_r = \frac{\pi w_0^2}{\lambda}. \tag{53}$$

Eliminating this influence from the measured spot sizes allowed us to calculate a divergence due to the optics of 0.066° for the green Nd:YAG beam and 0.0079° for the yellow dye beam. These small divergences allowed for the CARS phase matching condition to be properly investigated.

The geometry of the overlapping beams results in an interaction region about 20 mm long, significantly longer than the crystal dimensions.

3.2.3.5 Experimental Setup 5

The detection equipment used in Experimental Setup 4 was replaced in order to obtain better intensity sensitivity (Fig. 14).

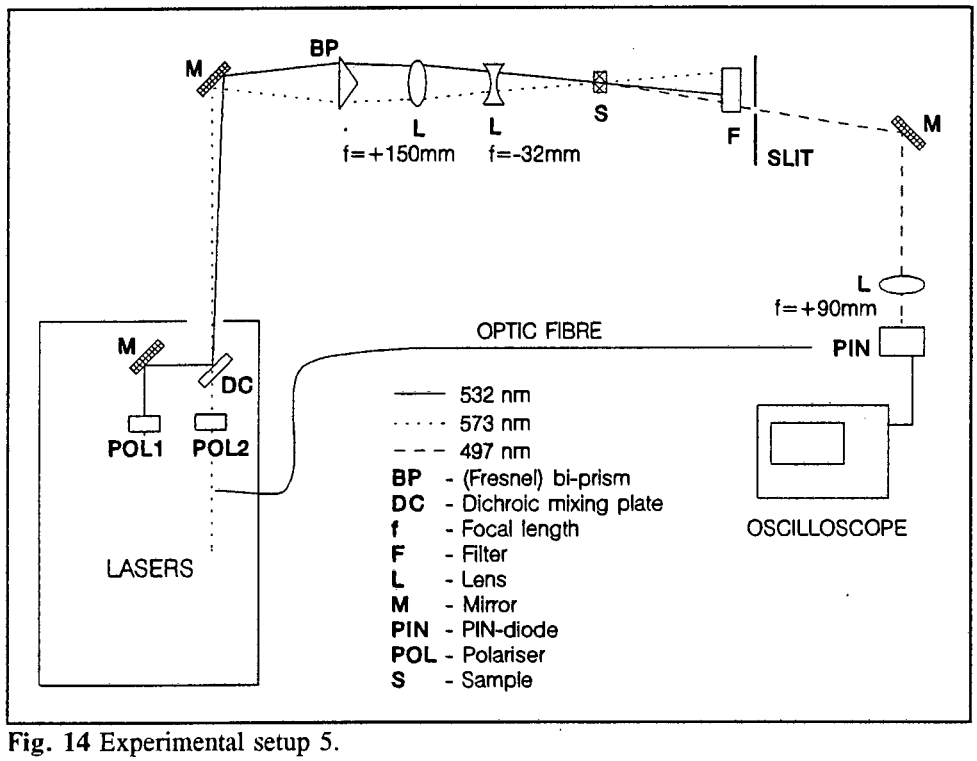

Fig. 14 Experimental setup 5.

A fast PIN-diode was used in place of the OMA and spectrometer, with its output being displayed on a Tektronix 2467 intensified 350 MHz oscilloscope. An optic fibre fed a time delayed portion of the Nd:YAG beam (split off from the laser) into the PIN-diode, producing a time-delayed pump intensity reference signal on the same oscilloscope trace for comparison purposes. A 90 mm focal length converging lens was used to focus the CARS signal onto the diode, since rotation of the sample meant that the CARS beam would move in a horizontal

plane (due to phase matching) with the change in crossing angle ϕ. A CCD camera was then mounted onto the oscilloscope to record the traces digitally.

A PC controlled the triggering of the laser and after a suitable time delay, the camera. The program Pulsed Laser Oscilloscope Program (PLOP) had previously been written by Allan Hanbury of the Laser Laboratory. At an interval of 1 s PLOP outputted a TTL pulse to the laser control system, triggering 1 Hz single laser shots. These laser pulses generated a CARS signal and this together with the Nd:YAG signal from the optic fibre was detected by the PIN diode and displayed on the analog Tektronix oscilloscope. Approximately 50 ms after the laser was triggered, another TTL pulse sent from PLOP to the CCD camera opened the camera shutter for 200 ms to capture the combined CARS and Nd:YAG signals. PLOP then downloaded the 8-bit greyscale TIFF image from the camera to the computer's hard disk before triggering the next laser shot. PLOP therefore provided us with the capability to use the analog oscilloscope as a digital storage oscilloscope. When the hard drive's capacity was fully utilised, PLOP ceased firing the laser and converted all the stored oscilloscope bit-mapped traces to numerical traces.

The oscilloscope initially was triggering on the electromagnetic noise of the laser capacitor banks, but this was eliminated by employing a double trigger. The oscilloscope was first triggered from the computer, after which a second delayed trace trigger ran, the delay selected being long enough for the electromagnetic noise to pass.

3.2.3.6 Experimental Setup 6

With the dichroic mixing plate in place, a modified Experimental Setup 3 was tried. This corresponds to that used by Levenson *et al.*[7], Fig. 15. The lasers' beam diameters are again shown and the beams are once more collinear upon leaving the laser table. They are reflected onto the optic bench, where they are focused onto the sample by a 150 mm focal length converging lens, before being collected by an identical lens. The short-wavelength pass filter reflects the green and yellow beams, transmitting the CARS signal which is reflected into the spectrometer. POL1 is a rotatable $\lambda/2$ plate and POL2 a fixed $\lambda/2$ plate. This configuration is very simple and easily produces the desired CARS signal. The input laser beams once again have a spread of $\boldsymbol{k}$ vectors in their profiles, with a set of these satisfying the phase

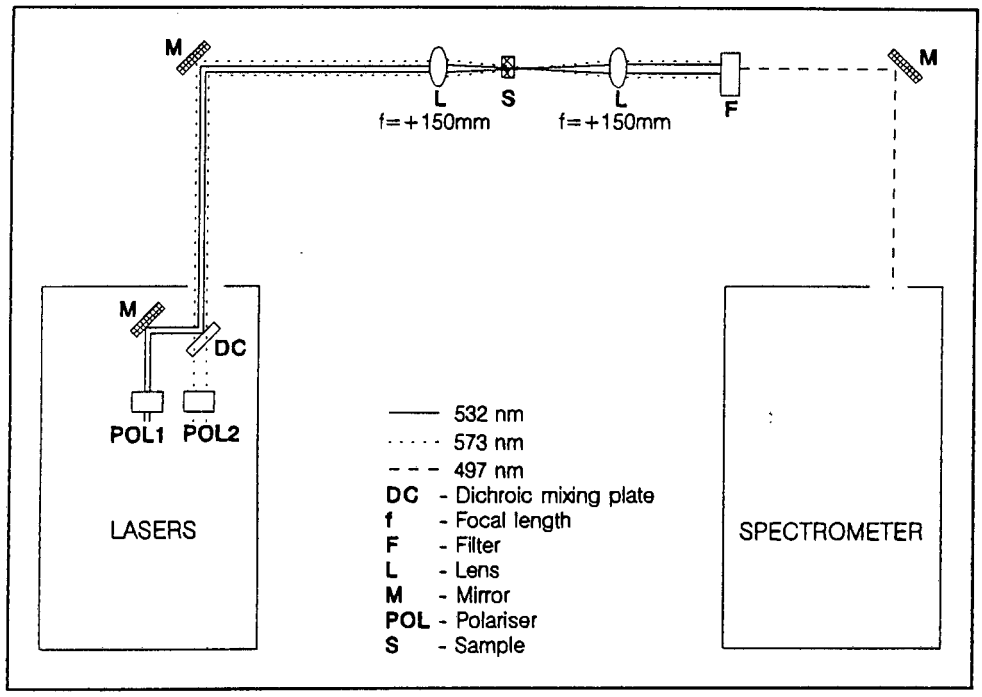

Fig. 15 Experimental Setup 6.

matching criterion. The transverse profile of the CARS signal upon leaving the sample is that of a cone, becoming a cylinder after the collecting lens. As discussed above, this setup is not ideal for probing the intensity sinc^2 dependence. Also, the CARS signal produced is $\sim$ 20 times lower in intensity than that produced by Experimental Setups 2,4 or 5.

Chapter 4
Results and Discussion

The various experiments performed during this study are now described. The results of these experiments and comparison of these results, where appropriate, with those reported in the literature are also presented. This chapter is divided into three sections. This first deals with the attempt to observe Stimulated Raman Scattering in diamond, the second with results deduced from the spectral data obtained, and the third with results inferred from the various CARS intensity investigations. This last section includes the investigation into the importance of phase matching in diamond, and polarization studies from which the ratio of the non-vanishing components of the cubic susceptibility tensor was determined.

4.1 Stimulated Raman Scattering (SRS)

As mentioned before, a narrowband Stokes source would improve the CARS intensity dramatically, and this was an incentive to demonstrate SRS in diamond. Using the Nd:YAG laser as pump, the SRS process would produce radiation at the (first-order) Stokes wavelength together with higher order ($\omega_1 + n\omega_R$) and anti-Stokes emissions ($\omega_1 - n\omega_R$). SRS in diamond has been reported by McQuillan *et al.*[29] using a giant-pulsed 30 ns ruby laser.

Experimental Setup 6 was used with the dye beam blocked off and a short-wavelength pass dichroic filter placed in front of the focusing lens, 20 cm from the diamond crystal. This formed half a cavity in order to enhance the SRS stimulation with the highly refractive polished diamond surfaces serving as part of this Raman resonator. The spectrometer was positioned at the first-order Stokes wavelength in the hope of observing this emission. On the vast majority of laser shots, no sustained SRS emission was observed. Increasing the laser intensity merely burnt holes on the sample surface. However, there were occasional

exceptional shots where a very strong SRS emission was observed. We believe that the reasons for this failure are two-fold:

(1) The occasional SRS emission was so large as to saturate our detector, suggesting that this was a result of a multi-mode laser shot. These mode beatings are $\approx$ 6 ns apart as opposed to the $\approx$ 17 ns pulse length of the SLM shots. We think that Stimulated Brillouin Scattering (SBS) rather than SRS was excited for the majority of pulses, except when the multi-mode pulse was of sufficiently high intensity. The Brillouin gain threshold would be reached before the SRS threshold due to the longer pulse times. Ramdas[33] measured the Brillouin shift in diamond to be 3 cm^{-1}. We could not confirm our suspicions that SBS was being favoured over SRS, as the Brillouin wavelength shift would be too small to separate from the (high intensity) Nd:YAG line without damaging the spectrometer grating. Acquiring a proper Fabry Perot étalon would confirm SBS, but this was deemed to require too many resources and would deviate from the focus of this study. The McQuillan study asserted that their ruby laser was single longitudinal mode, though we have to doubt this claim in the light of our own findings and the date when their work was performed.

(2) McQuillan *et al.* also reported that the SRS threshold was $\sim$ 1100 MW/cm^2. This high threshold requirement for SRS was also remarked upon by Nibler and Knighten[15]. We managed to reach $\sim$ 100 MW/cm^2 before the crystals were damaged and believe this inability to extend the laser intensity without damaging the diamond was due to the crystal polishing not being up to optical standard. It was apparent that the roughness of the crystal surface played a dominant part in determining their damage threshold. Increasing the intensity above this value in the hope of at least seeing an SRS signal in the single laser pulse it took to damages the surface, was in vain.

It is the combination of the above two factors that contrived to prevent us observing an SRS emission from diamond.

We then attempted to destroy the mode stability of the Nd:YAG laser by adjusting the cavity's optical length. We inserted a block of quartz into the cavity and rotated it while watching the time profile of the laser pulse on the oscilloscope (see Experimental Setup 5). All this accomplished was the reduction of the laser power. Adjusting the short étalon in the cavity also proved to be futile, and the drastic step of removing it altogether was then taken. The only axial mode selection component left was thus the long FP étalon, which formed one end of the cavity and therefore could not be adjusted. To our surprise the oscilloscope showed the laser pulses to still be single longitudinal mode. Further analysis of the effect of the étalon within the cavity confirms this. With reference to Fig. 6, elimination of the short étalon curve yields a laser mode structure shown in Fig. 16. Again one mode will reach cavity gain threshold first, and be amplified as the others are extinguished.

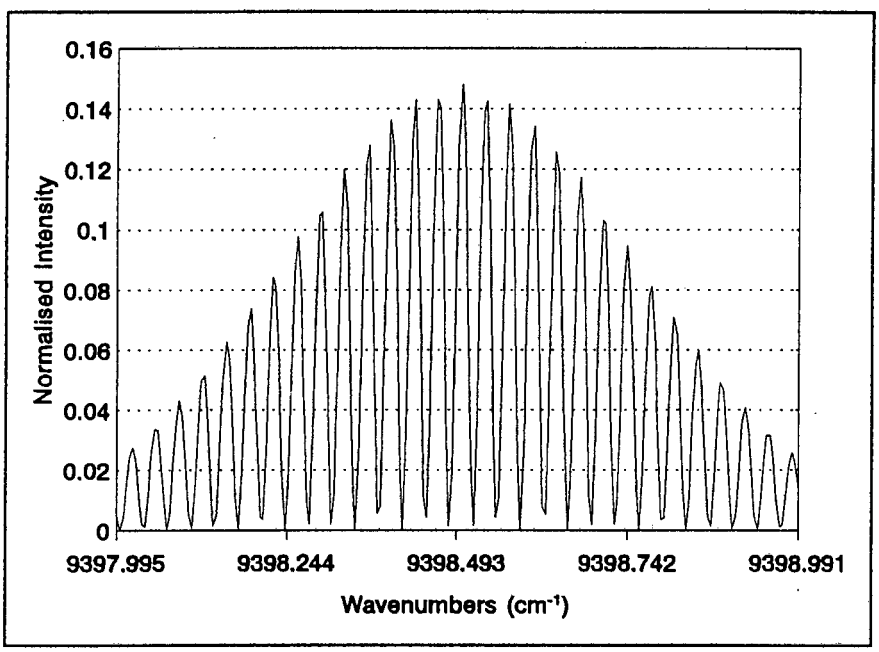

Fig. 16 Modulated Nd:YAG cavity modes with short Fabry Perot étalon removed.

Hence we were not able to produce multi-mode laser pulses at will, and could not test our hypothesis regarding the time-dependent gain threshold of Stimulated Brillouin versus Stimulated Raman Scattering. The failure to exhibit SRS in diamond was disappointing, and it seems that a multi-mode laser would be more suited to this process. Alternatively, if one used an actively Q-switched SLM laser with electronic synchronization of the cavity (such

as one from Light Wave Technologies), it would be possible to switch off the electronics and establish multi-mode operation.

4.2 Spectral information

Many of the experiments performed in this study utilised the spectrometer for measuring the CARS signal intensity. This provided an abundance of spectral data with which to analyze the lineshape, linewidth and Raman shift of the CARS signal. In particular, data from experiments using Experimental Setup 2 was used to determine the lineshape characteristics and provide information on the resonant χ_R and non-resonant χ_{NR} susceptibilities, while the Raman shift ν_R was determined using Experimental Setup 4. We could also directly record a spectrum for the Nd:YAG laser. This was crucial to this analysis, since it allowed ω_R, and therefore ν_R, to be measured through Eq. (3), and allowed the instrumental linewidth function of the detector to be determined.

The Raman shift ν_R was determined using Experimental Setup 4. The spectrometer was first calibrated using the strong 435.8 nm and 546.1 nm lines[34] from a Hg lamp. These lines were used since they were the only strong lines available in our region of interest, i.e. containing ω_1 and ω_3. The spectrometer optics, which comprised a lens to focus the dispersed light onto the OMA, was adjusted to minimise the widths of both the Hg wavelengths' spectral lines reasonably well. Total minimising of either of these wavelengths, degraded the linewidth and lineshape of the other, so that a compromise focal position of the lens was obtained. The spectrometer is designed so that its slit plays no part in obtaining a narrow spectral profile, other than to eliminate stray light.

The pump Nd:YAG light was then recorded (see Fig. 17), followed by the CARS signal. Adjustments were made for the dispersion of the spectrometer grating at the pump and CARS wavelengths. Using the angle through which the grating was rotated in measuring the pump and CARS spectra, together with the grating dispersion relation which is a function of this angle, we were able to obtain a value for ν_R. A final adjustment for the relative position of the two peaks on the 1024 pixel OMA, provides a value of $\nu_R = 1332.8 \pm 2.0\ cm^{-1}$ for the

Raman shift. This agrees favourably with the Raman shift quoted for diamond in the literature[28,7,29,30]. Titkov *et al.*[14] reported a new Raman line for brown diamond at a wavenumber shift of 1328 cm^{-1}. They ascribed this new line to plastic deformation of the crystal, probably as a result of the large number of dislocations present in their sample. The CARS spectra recorded by us covered a large enough wavenumber range to include this new line. This 1328 cm^{-1} was not observed in any of our diamond samples. This reported line could therefore be unique to brown diamonds, or as asserted, due to plastic deformation of the crystal.

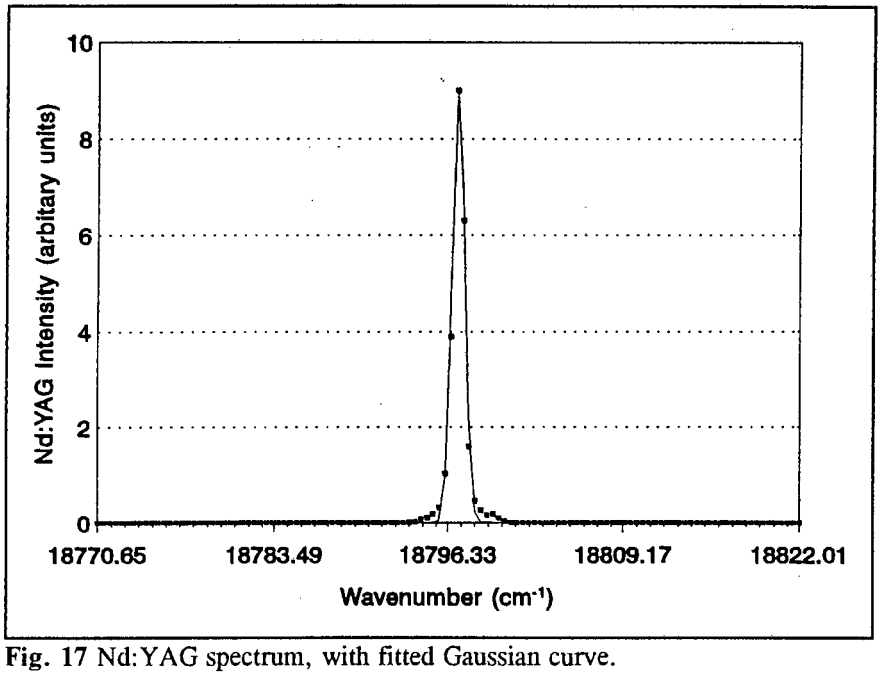

Fig. 17 Nd:YAG spectrum, with fitted Gaussian curve.

A typical CARS wavenumber spectrum is shown in Fig. 18. A visual inspection of the spectrum suggests that the lineshape obeys Eq. (37). The Lorentzian nature of the spectrum is expected from the outline of the CARS theory and in particular the resonant behaviour of the process. Fig. 18 also show an asymmetry in the spectrum, with a diminishing tail evident. However, there does not appear to be a large non-zero baseline present, implying that the non-resonant susceptibility χ_{NR} is small in comparison to the resonant susceptibility χ_R. We are also led to this assumption by Levenson and Bloembergen[8], who reported a value for the resonant susceptibility of diamond two orders of magnitude greater then the non-resonant values they calculated.

Thus we expect the second and third terms in Eq. (37), to be dominant in fitting a curve to the CARS spectrum, and the influence of the first term to be negligible.

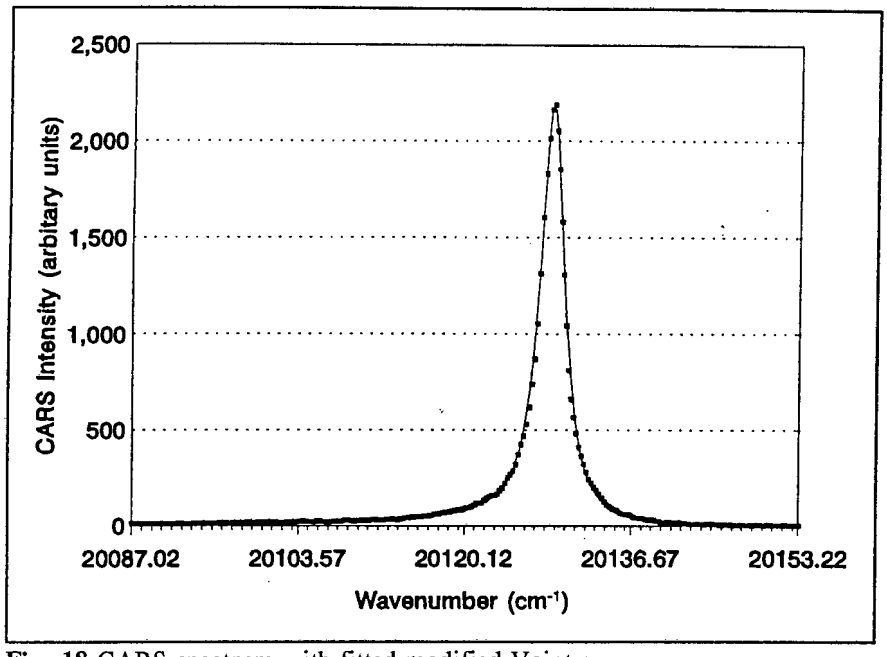

Fig. 18 CARS spectrum with fitted modified Voigt curve.

We therefore expected the CARS signal to fit as

$$\begin{aligned} L' &= \frac{2\chi_{NR}\chi_R}{\omega^2 + \Gamma^2}\omega + \frac{\chi_R^2}{\omega^2 + \Gamma^2} \\ &= \frac{1}{\omega^2 + \Gamma^2}\left(1 + \omega\chi_{ratio}\right) \\ &= L\left(1 + \omega\chi_{ratio}\right), \end{aligned} \tag{54}$$

where the Lorentzian profile has been identified as L, and χ_{ratio} is the ratio of the non-resonant to resonant parts (multiplied by two) of the third-order susceptibility.

The influence of the OMA detector in terms of the detector noise, first had to be taken into account. The green Nd:YAG light has a linewidth of 195 MHz corresponding to a wavenumber of 0.0065 cm^{-1}. Its spectrum should therefore appear as a single unbroadened line, since the OMA has a dispersive resolution of 0.2195 cm^{-1} at the green wavelength of 532 nm. However, it is obvious from Fig. 17 that this is not the case. The spectrum is therefore that of the detector response. We fitted a Voigt profile, i.e. the convolution of the Gaussian and Lorentzian profiles,

$$V(\omega) = \int_{-\infty}^{\infty} e^{-\frac{(\omega-\epsilon)^2}{2B^2}} \frac{1}{\epsilon^2 + A^2} d\epsilon, \tag{55}$$

to the Nd:YAG spectrum and obtained an excellent fit to the Nd:YAG data. Note that we have set $\Gamma = A$ as this is the variable name used in the curve fitting program. The curve fitting was performed by software written by Professor Gerald Robertson in Fortran and executed on a Intel based PC. This program implemented the Levenberg-Marquardt non-linear least squares fitting algorithm, and its operation will be discussed below. This program made use of the Harwell library of subroutines, as did the other curve fitting software mentioned later in this section.

The program reported that the Nd:YAG radiation had a Gaussian linewidth (FWHM) of $0.676 \pm 4.33 \times 10^{-3}$ cm^{-1}, convoluted with a Lorentzian of linewidth (FWHM) $0.264 \pm 4.56 \times 10^{-3}$ cm^{-1}. We now expected the measured CARS spectrum to be a convolution of this detector response V, and L' i.e.,

$$I_3(\omega) = V(\omega) * L'(\omega). \tag{56}$$

Two approaches presented themselves in trying to fit this function to the spectral data. A deconvolution of the measured spectrum I_3 could be performed, whereby the Voigt profile is divided out of the data, leaving the CARS signal L'. This has the disadvantage of introducing noise into the CARS spectrum, since the deconvolution would be performed numerically. The second method, and the one that was implemented, involves making use of the fact that the Fourier transform of a convolution of two functions is just the product of the Fourier transforms of the functions,

$$\mathcal{F}\{I_3\} = \mathcal{F}\{V\} \times \mathcal{F}\{L'\}. \tag{57}$$

Now the Fourier transform of the Voigt profile V is, making using of Eq. (55),

$$\begin{aligned}\mathcal{F}\{V(\omega)\} &= \frac{1}{2}\left[\frac{1}{2\pi A}\right]\frac{B}{\sqrt{(2\pi)}}e^{-\frac{1}{2}\left(\frac{B}{\pi}\right)^2 t^2}e^{-\frac{A}{2\pi}|t|} \\ &= \frac{B}{2A(2\pi)^{1.5}}e^{-\frac{1}{2}\left[\frac{A}{\pi}|t| + \left(\frac{B}{\pi}\right)^2 t^2\right]},\end{aligned} \tag{58}$$

that is just the product of the Fourier transforms of the Gaussian and Lorentzian functions. Since the inverse Fourier transform of

$$S = e^{-A|t|}, \tag{59}$$

is (ignoring scaling constants)

$$\frac{1}{i\omega + A} = \frac{A - i\omega}{\omega^2 + A^2}. \tag{60}$$

we see that the Lorentzian L is only the real part of this inverse Fourier transform.

A closer look at L' reveals that its Fourier transform is nothing more than $\mathrm{Re}\{\mathcal{F}^{-1}\{S\}\} + \chi_{ratio} \times \mathrm{Im}\{\mathcal{F}^{-1}\{S\}\}$, where Re{} and Im{} are the real and imaginary parts of their arguments. This form of representing L' is convenient since the Voigt fitting program used on the Nd:YAG data utilises the Fourier transform ideas to perform the Gaussian-Lorentzian convolution. The Levenberg-Marquardt routine employed in the Voigt fitting program, has as its input the parameters to be fitted i.e. A and B, the function to be fitted i.e. the convolution V, and the derivatives of this function with respect to the parameters. The input function is now the convolution given in Eq. (55), impossible to represent analytically so that it is rather expressed as the inverse Fourier transform of Eq. (58). Thus in a sense the parameters A and B are fitted to Eq. (58); the inverse Fourier transform of this is taken with only the real part of this used, in order to isolate only the Gaussian and Lorentzian components. The result is the function V, which is passed to the Levenberg-Marquardt routine together with the appropriate partial derivatives.

The only difference in fitting a Voigt function and the measured CARS function I_3, is then to incorporate the previously discarded imaginary part of the inverse Fourier transform of S with the original Voigt being fitted, and pass this to the Levenberg-Marquardt routine.

Data taken from one of the polarization studies, where the polarization of the Nd:YAG beam was changed while the dye beam was kept horizontally (relative to the laboratory frame) polarized, was used to fit the modified Voigt function described above. The full linewidth at half-maximum of the CARS signal, was calculated from the parameter A returned by the curve-fitting function, for each polarization state. The ratio of the resonant and non-resonant parts of the susceptibility $\chi^{(3)}$, was also returned by the curve-fitting routine, for each polarization condition. These results are listed in Table 1. The data and fitted curve in Fig. 18 are for the Nd:YAG polarization equal to 20°.

Table 1 : List of full linewidths at half-maximum of the CARS signal, and ratio of resonant and non-resonant parts of the cubic susceptibility, as a function of pump beam polarization. Certain polarization conditions were repeated as part of this experiment, due to low intensities being measured at these points.

Nd:YAG Polarization (degrees)	Lorentzian linewidth (FWHM) A (cm^{-1})	A Standard deviation	$\frac{\chi_{NR}}{\chi_R}$ (s)	χ_{ratio} Standard deviation
0	2.371	0.012	-0.032	0.010
10	2.488	0.007	-0.026	0.006
20	2.407	0.010	-0.029	0.008
30	2.390	0.012	-0.031	0.010
40	2.503	0.013	-0.027	0.010
50	2.395	0.011	-0.032	0.008
50	2.337	0.015	-0.027	0.012
60	2.366	0.013	-0.021	0.010
60	2.293	0.016	-0.028	0.014
70	2.332	0.012	-0.026	0.010
70	2.358	0.010	-0.028	0.008
70	2.354	0.009	-0.014	0.008
80	2.333	0.015	-0.027	0.012
80	2.401	0.015	-0.028	0.012
80	2.361	0.011	-0.030	0.010

Nd:YAG Polarization (degrees)	Lorentzian linewidth (FWHM) A (cm^{-1})	A Standard deviation	$\frac{\chi_{NR}}{\chi_R}$ (s)	χ_{ratio} Standard deviation
90	2.360	0.013	-0.027	0.010
90	2.290	0.010	-0.031	0.008
90	2.584	0.010	-0.021	0.008

The average full linewidth across all listed polarizations is 2.385 cm^{-1} (therefore half-width equals 1.192 cm^{-1}) with a standard deviation of 0.0742 cm^{-1}. Similarly, the average of the ratio χ_{NR}/χ_R = -0.0278 s with standard deviation of 0.0045 s. The measured linewidth agrees very favourably with that reported for spontaneous Raman scattering in the literature. Washington and Cummins[30] measured a half-width of 1.2 $\pm$ 0.2 cm^{-1} for their spontaneous scattering experiments, while Levenson and Bloembergen[8] used a half-width of 1.04 cm^{-1}. The ratio of the susceptibility components is of the same order of magnitude as that reported by Levenson, Flytzanis and Bloembergen[7]. They obtained a value for this ratio (actually they calculated the reciprocal of this ratio), when both the laser electric fields where polarized along the [110] crystal direction, of 0.0476. They also state[8] that non-linear susceptibility data is frequency dependent, and that one must take care when comparing such data at different frequencies. Not having the instrumental sensitivity to repeat their measurements of the non-resonant susceptibility components, we cannot directly compare our result of the susceptibility ratio at a single frequency with their calculation of the various components at different frequencies. We must therefore be satisfied with this order of magnitude agreement.

4.3 Intensity measurements

This section presents the experiments performed, where the recorded data are intensity rather than spectral measurements. This includes the dependence of the CARS signal intensity on the intensities, polarization, and degree of phase matching of the lasers' intensities. The polarization data also allows the ratio of the two non-zero cubic susceptibility tensor components, to be estimated. Firstly though, experimental consideration that affect the

measured intensities must be discussed. These factors are the neutral density filters used, the fluctuations of the laser and the reasons for this, and the movement of the crystal relative to the laser beams.

4.3.1 Neutral density filter calibration

In the course of the our experiments, neutral density filter were utilised in the attenuation of the laser beams and CARS signal. A calibration of these filters and one combination of them, was undertaken to accurately establish their attenuation factors. Only the attenuation of the CARS beam was measured, as the majority of this study deals with relative intensities only.

Experimental Setup 5 was used. Neutral density (ND) filters NG3 D1.0 and NG5 D0.3 were placed in the path of the green beam, and ND filter NG5 D0.6 in the yellow beam. These lowered the input intensities to the sample, to produce a CARS signal that was usable over the range of filters being tested. The absolute laser intensities were not important, as the attenuation factor is unity, less the ratio of transmitted and incident intensities. Both the lasers' radiations were vertically polarized. The unattenuated CARS beam power was first recorded, whereafter the ND filters were inserted in this beam and these powers recorded. At the end of the sequence of filters, the unattenuated beam was again recorded for comparison purposes. 60 shots were recorded at each setting with the first 10 being discarded. The first 10 shots were omitted from the analysis, as previous work performed in this laboratory has shown the Nd:YAG laser's power to stabilise only after this number of shots[35]. This is due to heating of the oscillator rod and cavity. Computer programs then determined the intensity of each shot by summing under the curves, these being averaged and the error due to laser fluctuations determined.

The average ND filter intensities were then divided by the unattenuated beam intensity, and 1 subtracted from these to produce the attenuation factors. The results appear in Table 2.

Table 2 : Attenuation factors for the neutral density filters used in the experiments.

Neutral density (ND) filter	Attenuation factor AF	Uncertainty in AF
NG5 D0.3	0.55	0.046
NG5 D0.6	0.33	0.020
NG5 D0.3 + NG5 D0.6	0.19	0.009
NG3 D1.0	0.16	0.007

The NG D0.3 and NG D0.6 results were confirmed by similar work performed previously in the Laser Laboratory.

4.3.2 Fluctuations of the lasers

Using Experimental Setup 5, the stability of the Nd:YAG and dye laser intensities were investigated. Both were horizontally polarized, with the unattenuated dye beam following the normal path and being focused onto the PIN-diode, while the optic fibre fed the green Nd:YAG light into the diode. Four laser power settings were selected and 60 dye and Nd:YAG shots recorded. The first 10 shots were again omitted from the analysis. A computer program was written to display the temporal spectra and record the peak values of the dye and Nd:YAG beams. This was used to approximate the intensity of the individual beams. Displaying the shots allowed multi-mode shots to be excluded from the set to be analyzed.

Averages and standard deviations were then calculated for each power setting, and the results show that the Nd:YAG beam intensity fluctuates with an uncertainty of $< 2\%$, and that the uncertainty in the dye's intensity is $< 4\%$. The addition of an interference filter into the dye laser cavity increased the dye intensity fluctuations, and was therefore not exploited. We were also able to show that the dye laser intensity varied proportionally with that of the Nd:YAG, by dividing the peak Nd:YAG intensity by that the dye's peak. This was done for all acceptable shots recorded, and the variation in this ratio was only 1.3%.

While these uncertainties might suggest that the CARS intensity should only vary at most by 4 to 5%, this is an incomplete picture of the CARS uncertainty. The dye laser spectral profile varies dramatically in terms of peak intensity and overall shape. Thus the I_2 contribution at ω_2 varies in an unpredictable manner, making the CARS intensity variation theoretically indeterminate.

The temporal overlap of the Nd:YAG and dye pulses might also be thought to affect the CARS intensity. The difference in dye and Nd:YAG temporal peak positions was recorded but this showed no discernible variation. The value of 0.037% obtained for this variation is largely attributable to the error in digitising the oscilloscope image. Overall then, the lasers' intensities are very stable but the dye spectral profile variation from shot to shot makes the predominant contribution to the CARS intensity fluctuation. The precise nature of this modulation requires the Nd:YAG and CARS intensities to be measured simultaneously with the dye spectral profile and intensity, so that a thorough understanding of the interaction can be sought.

4.3.3 Movement of crystal in beam path

As a prelude to the investigation of the CARS phase matching condition, changes in the CARS intensity due to movement of the diamond crystal along the beam propagation and transverse to this direction were scrutinised. Experimental Setup 5 was used. To investigate the CARS dependence transverse to the laser beams propagation, we first produced a CARS signal from the crystal. The crystal was then moved so that the laser beams passed through near one edge of the crystal. Sixty shots were recorded, with the first 10 excluded. The crystal was then moved (transversely) so that the beams passed through a different region, and 60 shots were again recorded. This process was repeated 7 times. The CARS intensity was estimated by summing under the curves of the recorded shots, after excluding the multi-mode shots, and the average of each set of 50 shots taken. No significant changes in the CARS intensity was found in the transverse direction.

For the direction along the beam propagation, a similar procedure was followed, with the only difference being the direction of crystal movement. The crystal was now moved in the

direction of the beam propagation. Within experimental agreement, the CARS intensity was constant, provided the crystal stayed within the laser beams' region of overlap. As the crystal moved out of the overlap region, the CARS intensity dropped rapidly. This enabled us to determine the position of the overlap region, and to ensure that the crystal was centred in this region in subsequent experiments.

4.3.4 CARS signal dependence on pump and Stokes intensities

From Eq. (18), we expected the CARS signal intensity to vary linearly with the dye laser intensity and quadratically with that of the Nd:YAG. The experimental investigation of these dependencies utilised Experimental Setup 2, with either the green (pump) or yellow (Stokes) intensities being individually attenuated and the CARS intensity measured. Both the input lasers were polarised horizontally, and the diamond was rotated to optimise the phase matching angle and produce the strongest CARS intensity.

The intensity of the Nd:YAG was reduced by the insertion of a neutral density filter, and the CARS spectrum measured with the dye intensity left unattenuated. Additional ND filters were inserted to further reduce the laser intensity, with the CARS spectrum being measured with each addition. Thirty shots were recorded for each ND filter. This entire procedure was repeated with the dye being attenuated and the Nd:YAG intensity unmodified. A computer program was written to obtain an estimate of the average CARS intensity and the standard deviation of this average. This was done by summing under the spectral curves for each set of 30 shots, and averaging these values. These intensities were then plotted in Quattro Pro with the independent variable being the filter factor (AF), and the programs linear regression facility used to fit the appropriate curves to the data.

For the CARS signal dependency on the dye intensity (Fig. 19), a straight line was obtained when CARS intensity vs. AF was fitted, with the correlation coefficient reported as 0.98. For the Nd:YAG dependence (Fig. 20), the linear regression was performed on CARS intensity vs. $(AF)^2$, and a correlation coefficient of 0.97 was obtained. These results confirm that the CARS signal intensity has a linear dependence with the Stokes intensity I_2, and a quadratic dependence with the pump intensity I_1.

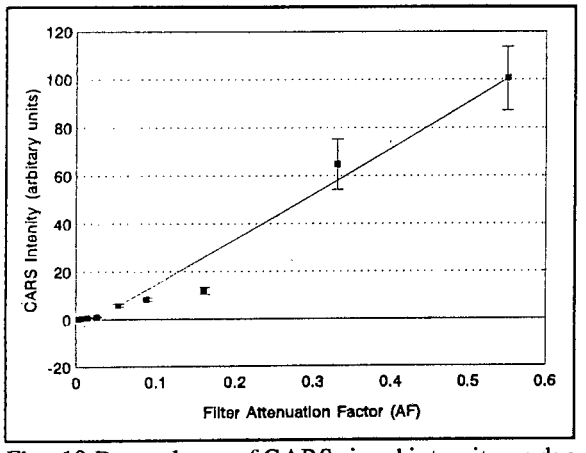

Fig. 19 Dependence of CARS signal intensity on dye intensity.

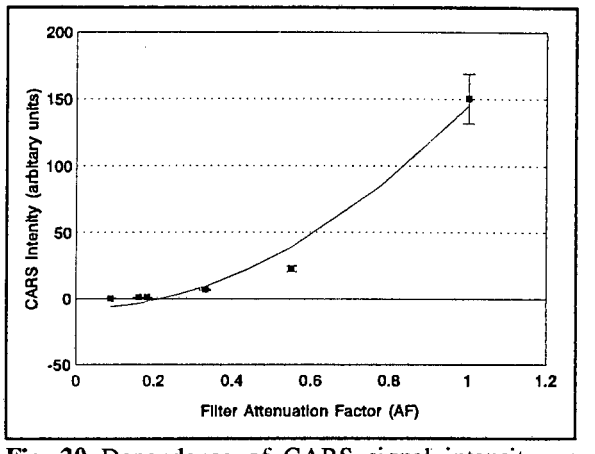

Fig. 20 Dependence of CARS signal intensity on pump Nd:YAG intensity.

4.3.5 Angular dependence of CARS signal

The phase matching condition in the form of the sinc^2 dependence of the CARS intensity, was experimentally investigated. Experimental Setup 5 was utilised, with both Nd:YAG and dye beams being vertically polarized (laboratory frame). These polarization conditions were chosen since the crystal would be rotated about the vertical axis (laboratory frame) to change the beam crossing angle, and we required the coupling of the electric fields E_1 and E_2 with χ_{CARS} (see Eqs. (16), (17) and (18)) to be constant. Any other polarizations would cause the CARS intensity I_3 to vary simultaneously as a function of the beam crossing angle and $I_1^2 I_2 |\chi_{CARS}|^2$, as (from Eq. (16)) the components of the laser electric fields along the crystal axes would vary with rotation of these axes, if the fields were not polarised along the axis of crystal rotation.

ND filters NG3 D1.0 and NG5 D0.3 attenuated the pump beam, with the dye beam left unattenuated. The diamond was placed in the sample holder, and the goniometer adjusted so that the crystal's front face was normal to the laser beams. This established the plane of refraction and reflection of the beams to be constantly horizontal with crystal rotation. The crystal was rotated in 1° increments from a small CARS signal, through the maximum intensity and onwards to a small signal again, with the angle between the Nd:YAG beam and the diamond surface normal δ_1, decreasing with these rotations. Care was taken to ensure that the position of the crystal in the beam propagation direction was the same with each rotation, and that the transverse position was also approximately the same.

Sixty intensity shots per angle were recorded, and the PLOP equipment allowed 8 angles to be recorded consecutively before the image storage facility was full. The images were then digitised and these oscilloscope traces stored, before the next batch of 8 angles were recorded. As a check for intensity fluctuations, the last angle was repeated, so that 3 data points are duplicated in the 31 intensities (angles) that were eventually measured. The intensity of each CARS and Nd:YAG shot was determined by summing under the individual curves. The first 10 shots per angle setting were excluded from the analysis. Each shot was also visually inspected and multi-mode shots excluded. An average intensity and standard deviation for both the CARS and Nd:YAG beams at each angle was calculated.

The CARS signal had to be adjusted to account for any fluctuations in the laser beam intensities. While the Nd:YAG intensities were simultaneously recorded, it was not possible with the existing equipment to record the dye laser intensity as well. In the absence of this information, the approximately linear dependence of dye laser intensity on Nd:YAG intensity was assumed, and the average CARS intensity was taken to be proportional to the cube of the Nd:YAG intensity. Due to the high index of refraction of diamond, $\simeq$ 17% of the incident light will be reflected. The transmission amplitude of the Nd:YAG and dye electric fields at the front diamond face, varies with incident angle and is given by

$$t_{\perp} = \frac{2n_i \cos\epsilon}{n_i \cos\epsilon + n_t \cos\delta}, \tag{61}$$

where ϵ is the angle of incidence, δ the angle of refraction, n_i & n_t the refractive indices of air and diamond respectively. The transmitted portion of the laser intensities is then $I_{1,2} t^2_{1,2\perp}$.

The adjusted CARS intensity is then

$$I_{3adj.} = \frac{I_3 t^2_{1\perp} t_{2\perp}}{I_2^3}. \tag{62}$$

We also needed to relate the beam crossing angle to Δk, since from Eq. (18), sinc^2 varies with this rather than θ. $\Delta \boldsymbol{k}$ is a vector quantity defined in Eq. (17), and is a result of the lasers' and CARS's wave vectors departing from the perfect phase matching condition (Fig. 2). This necessitates three geometrical situations to be considered to account for all possible contributions to Δk.

4.3.5.1 Angular change, k_1 & k_2 constant

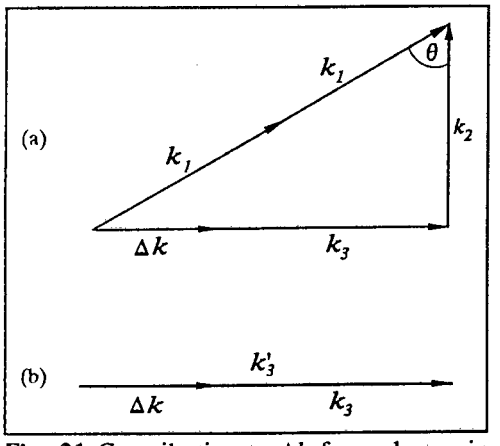

Fig. 21 Contribution to Δk from change in beams crossing angle.

We first consider the contribution to Δk from only a change in θ, with the Nd:YAG and dye wave vectors unchanged. Since phase matching is equivalent to momentum conservation, a closed vector triangle (Fig. 21 (a)) must always result when the wave vectors are added. For the enhancement of the coherent process, we require that Δk be minimised. This implies that Δk and k_3 be parallel, and we denote this sum k'_3 (Fig. 21 (b)). Thus $\Delta k = k'_3 - k_3$, and simple mathematics gives

$$k'_3 = \sqrt{(2k_1)^2 + k_2^2 - 2(2k_1)k_2\cos\theta} \; . \tag{63}$$

Since k_1, k_2 and k_3 are known, Δk can be calculated for any beams crossing angle θ.

4.3.5.2 Fixed beams crossing angle θ, variation in k_2

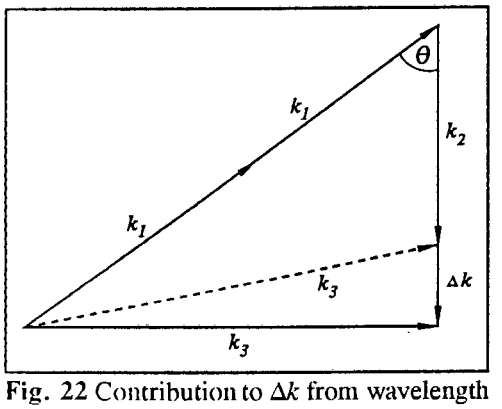

Fig. 22 Contribution to Δk from wavelength spread as a result of broadband dye spectrum.

Because the dye laser is a broadband source, the length of wave vector k_2 can change by a factor Δk so that $k_2 + \Delta k$ corresponds to a one of the wavelengths in the broad dye spectral emission. The maximum possible Δk then corresponds to the dye linewidth. However the CARS signal requires Eq. (3) to be satisfied, restricting the choice of $k_2 + \Delta k$. In fact, only if the $\hbar(\omega_1 - \omega_2)$ energy state (Fig. 1) is broadened energetically, will Δk be non-zero. The CARS spectral data collected indicates a narrow linewidth, suggesting that the energy state is in fact not broadened and that $\Delta k = 0$ for all practical purposes. Note that the Nd:YAG spectrum is so narrow that any variation in k_1 can strictly be ruled out.

4.3.5.3 Divergence of beams

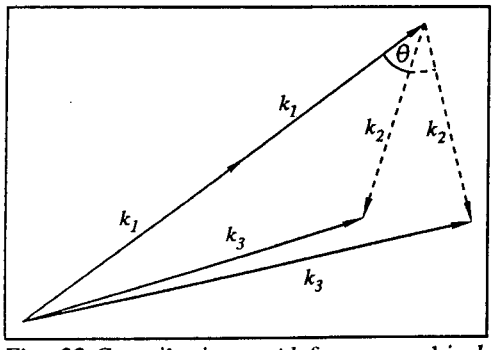

Fig. 23 Contribution to Δk from spread in k vector as a result of beams' divergence.

For any divergence of the laser beams in the interaction volume, a spread or set of wave-vectors Δk will exist in each beam. Each k_1 wave-vector then interacts with each k_2 wave-vector, so that I_3 is then a sum over all these intensity contributions. It is then very difficult to ask what θ is, and this situation must be avoided. The divergence in our beams at the crossing point is very small, making any contribution to the uncertainty in θ, and therefore Δk, negligible. Fig. 23 is simplified to show only a divergence in k_2, while the full picture involves divergences in both laser beams as discussed here.

Δk is then only influenced by changes in θ, and making use of Eq. (63), the recorded angles were converted to their appropriate Δk values. Since the phase matching sinc^2 factor is a function of both Δk and L, the variation in the length of the interaction region had to be accounted for. This length L can be taken to be the length of the Nd:YAG beam in the crystal. L varies with the rotation of the crystal, and is related to the thickness of the crystal L_0, i.e. the perpendicular distance between the parallel faces, by $L = L_0/\cos(\epsilon)$.

A plot was made of the adjusted CARS intensity $I_{3adj.}$ versus Δk, together with the corrected uncertainties. The Origin program, through the use of its Levenberg-Marquardt non-linear least squares fitting algorithm, was employed to fit a $\text{sinc}^2(\Delta kL/2)$ curve to these data points. The plot of the data points and the fitted curve is shown in Fig. 24.

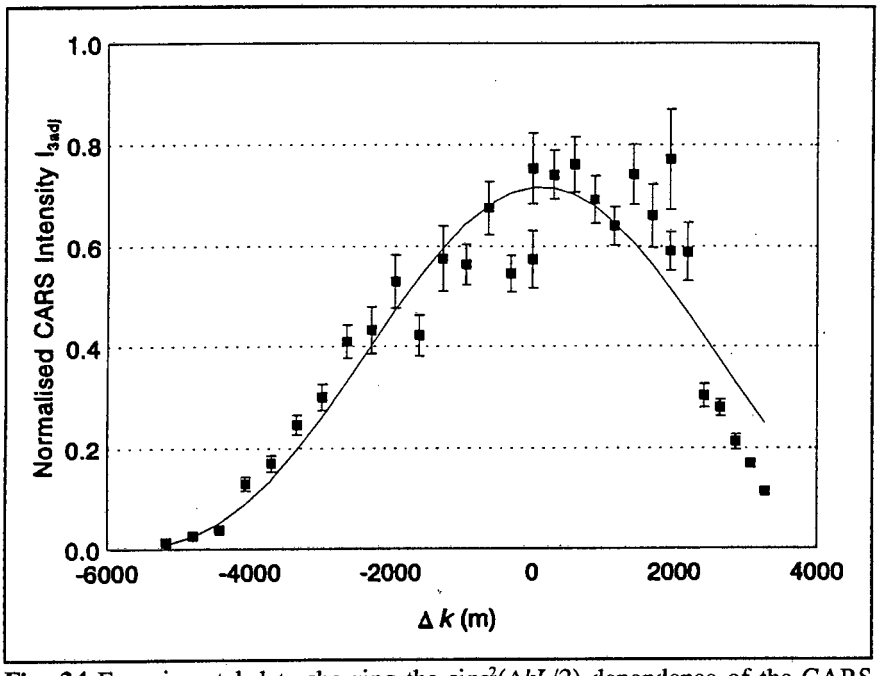

Fig. 24 Experimental data showing the $\text{sinc}^2(\Delta kL/2)$ dependence of the CARS signal. Δk is due only to changes in laser beams' crossing angle i.e. phase matching angle. The solid line is the fitted curve.

The algorithm returned a best estimate for the width of the crystal of $L_0 = 1.07 \pm 0.06$ mm. This corresponds to the measured width of the sample used very well. The fit of the theoretical sinc^2 function to the data points is good, and confirms the requirement for good phase matching in order to generate a CARS signal. The fluctuations in some of the data points are as a result of the mixing of the laser beams as discussed above (§ 4.3.2).

4.3.6 χ^3 components

It has already been theoretically established that the third-order susceptibility tensor χ^3 has only 2 non-zero components. In order to gain some information on these components (and therefore the susceptibility), polarization studies were performed. From Eq. (16), it is clear that changing the polarization of the input electric fields (laser beams) alters the CARS signal polarization and intensity. The experiments performed involved measurement of the CARS intensity, and in one case CARS polarization, as the lasers' polarizations were altered. Only relative values for the χ^3 components could be deduced, since determination of their absolute values would require simultaneous knowledge of both lasers' and CARS intensity and spectral interaction in order to accurately demodulate these from the CARS fluctuations. This problem has already been discussed above (§ 4.3.2).

We first need to express theoretically the form of the CARS intensity and polarization condition as a function of the input electric fields' polarizations, so that the experimental results can be discussed meaningfully.

Experimental Setups 2, 4 & 5 were used to gather the polarization data and in all cases, the geometry of the electric field interaction with the diamond crystallographic axes, and therefore the susceptibility, is the same. Using the fact that the diamond's polished face is the (110) crystal plane, Fig. 25 illustrates this geometry.

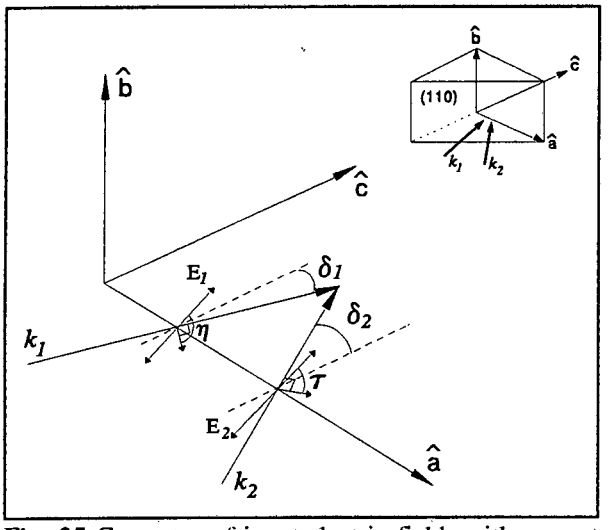

Fig. 25 Geometry of input electric fields with respect to the crystal axes.

From this diagram, the Nd:YAG laser electric field is expressed in component form as

$$\boldsymbol{E}_1 = E_1\cos\eta\cos\delta_1\hat{a} + E_1\sin\eta\hat{b} + E_1\cos\eta\sin\delta_1\hat{c}, \tag{64}$$

and the dye laser electric field as

$$\boldsymbol{E}_2 = E_2\cos\tau\cos\delta_2\hat{a} + E_2\sin\tau\hat{b} + E_2\cos\tau\sin\delta_2\hat{c}. \tag{65}$$

Note that $\delta_1 + \delta_2$ equals the beams crossing angle so that the maximum value either of these angles can have is $\sim 1.5°$. Eqs. (64) and (65) are then approximated by

$$\begin{aligned} \boldsymbol{E}_1 &= E_1\cos\eta\hat{a} + E_1\sin\eta\hat{b} \\ \boldsymbol{E}_2 &= E_2\cos\tau\hat{a} + E_2\sin\tau\hat{b}. \end{aligned} \tag{66}$$

The CARS signal polarization components can then be written, from Eq. (16), as

$$\begin{aligned} P_a &= 3(\chi_{abba}\sin^2\eta\cos\tau + 2\chi_{abab}\sin\eta\cos\eta\sin\tau)E_1^2E_2 \\ P_b &= 3(\chi_{baab}\cos^2\eta\sin\tau + 2\chi_{baba}\cos\eta\sin\eta\cos\tau)E_1^2E_2. \end{aligned} \tag{67}$$

The form of the CARS intensity as an explicit function of these electric field polarizations is then

$$I_3 \propto E_3^2 \propto P^2 = P_a^2 + P_b^2. \tag{68}$$

Figs. 26 - 29 show CARS intensity I_3 plotted against Nd:YAG polarization η. By analysis of these curves we are able to estimate the ratio χ_{abba}/χ_{abab}, and the parameter τ simultaneously. A value for the unknown angle τ, the dye laser polarization with respect to the crystal axes, is constant within an experiment but differs from one experiment to another.

The polarization of the CARS signal is complicated by the fact the diamond is a cubic crystal, so that all crystal axes are indistinguishable. However, we have chosen to measure the angle of the CARS polarization vector relative to one of these axes and have therefore introduced an asymmetry into the geometry. This is evident from Eq. (66) where $P_a \neq P_b$ in general. Thus the CARS vector polarization angle we measure experimentally will be either

$$\arctan\left[\frac{P_a}{P_b}\right], \tag{69}$$

or

$$\arctan\left[\frac{P_b}{P_a}\right], \tag{70}$$

with the actual measured values determining which form is correct.

Two CARS intensity and one CARS polarization data sets were recorded with Experimental Setup 2. The dye laser was polarized horizontally (using POL2) with respect to the laboratory, with the Nd:YAG polarization initially also horizontal. The crystal was initially rotated to provide a strong signal which was then recorded using the spectrometer. Thirty shots per polarization state were recorded. The green beams polarization was then changed

by rotating the λ/2 plate (POL1) and this signal recorded. This procedure was followed until the Nd:YAG was polarized vertically with respect to the laboratory. The entire experiment was repeated with a second sample. None of the electric fields were attenuated. A computer program then displayed the individual shots, before summing under the curves to estimate the intensity and averaging these. The error in these average intensities were then estimated by their standard deviations. The Origin program's Levenberg-Marquardt routine was then used to fit Eq. (68) to these averaged intensities. The recorded data and best-fit curves for the two samples, denoted PD1 and PD2, are shown in Fig. 26 and Fig. 27.

The variation of the CARS polarization as a function of the Nd:YAG polarization was also recorded using this experimental arrangement, with the Glan-Thompson polarizer (POL3) employed to find a minimum in the transmitted CARS signal. At this minimum, the CARS electric field must be perpendicular to the Glan-Thompson transmission axis, thus the CARS polarization angle could be measured. The recorded data was then visually found to fit Eq. (70). Attempts to obtain a best-fit curve of Eq. (70) to the data PD5, proved fruitless. This was as a result of the ambiguity in the arctan function, since this maps its argument to the first or fourth quadrant (between -90° and +90°) only.

In order for the curve fitting program to obtain any reasonable fit to the data points, this ambiguity had to be avoided. This could only be achieved by the inclusion of conditional statements which re-mapped the arctan output to the full 360° plane. These conditional statements meant that the derivatives needed by the curve fitting program were impossible to determine analytically. Attempting to calculate these derivatives numerically, resulted in the curve fitting program producing unreasonable fits, with the standard deviation of the fitted parameters being comparable to the parameter values. Various other curve fitting routines were attempted, with no improvement in the standard deviation. In some cases, the standard deviations were even larger than the fitted parameters. The only resolution to this problem was to use the average of the parameters (see Table 3), determined after performing the curve fitting to all the other polarization data PD1-PD4, to fit the arctan function to PD5. The data and this curve are shown in Fig. 30.

Experimental Setup 4 was used to repeat the CARS intensity dependence on input electric field polarization measurement. ND filters NG3 D1.0 and NG5 D0.6 attenuated the Nd:YAG and CARS beams respectively. The crystal was rotated to produce a strong CARS signal, after which the dye was polarized horizontally (using POL2). Again, we began with the Nd:YAG horizontally polarized (using POL1), adjusting this polarization until the green beam's polarization was vertical. Thirty shots of the CARS spectra were recorded at each green beam polarization angle. This data PD3 was processed as before, and the results are shown in Fig. 28.

Finally Experimental Setup 5 was used to record the CARS signal intensity versus Nd:YAG polarization data. The procedure was the same as above, except that the dye beam was polarized vertically using the Glan-Thompson polarizer, and the green beam polarization set initially vertical and rotated towards the horizontal. ND filters NG3 D1.0 and NG5 D0.3 attenuated the Nd:YAG signal, while various filters were used diminish the CARS intensity whenever this was needed. Another program was written and used to plot the time spectra so that multi-mode shots could be excluded. Intensities (by summing under the curves) and standard deviations were again calculated, this time for both recorded CARS and Nd:YAG signals. The AF filter factors were used to adjust for the reduction in CARS signal strength, before the averaged CARS intensities were adjusted for laser fluctuations by dividing these by the cube of the Nd:YAG intensity averages. A best-fit curve was obtained as before and this is presented in Fig. 29 along with the data (PD4).

It was found that the Nd:YAG laser beam was elliptically polarized before entering the crystal. This was due to the dielectric coating of the mirror(s) used to deviate the light into the sample. This polarization condition was not a significant difficulty as the deviation from pure linear polarization was small, i.e. the component normal to the POL1 transmission axis was small.

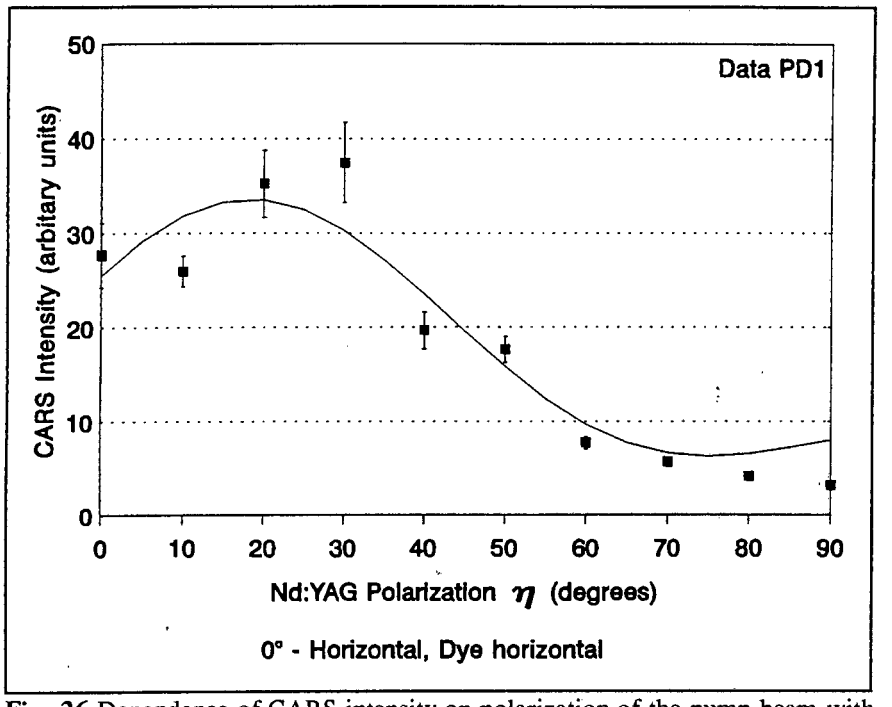

Fig. 26 Dependence of CARS intensity on polarization of the pump beam with both the pump and dye beams initially horizontal in the laboratory frame. The solid line represents the fitted curve.

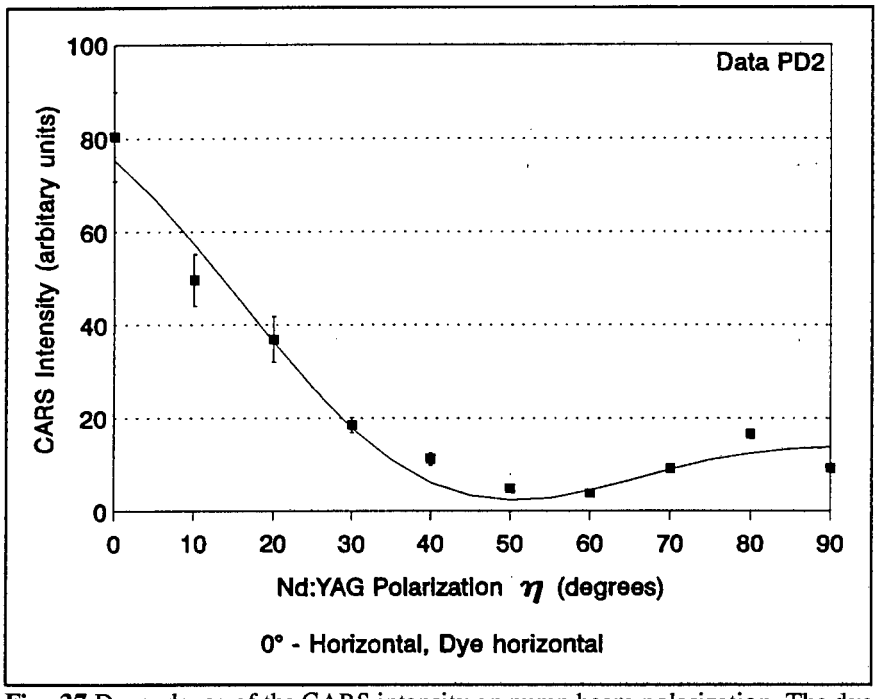

Fig. 27 Dependence of the CARS intensity on pump beam polarization. The dye radiation was horizontally polarized, as was the pump, initially. The solid line represents the fitted curve.

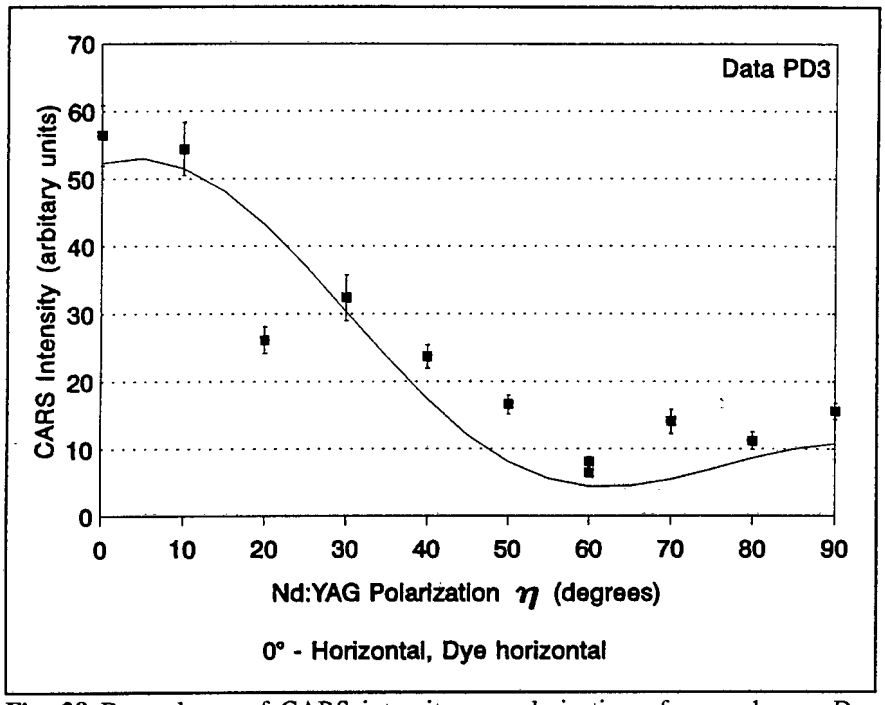

Fig. 28 Dependence of CARS intensity on polarization of pump beam. Dye horizontally polarized. The solid line represents the fitted curve.

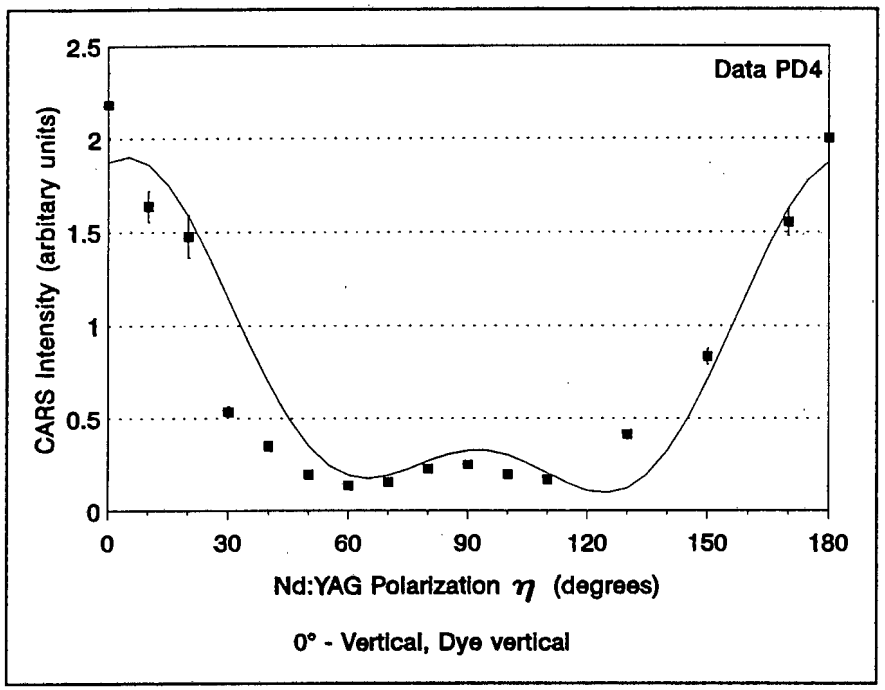

Fig. 29 Dependence of CARS intensity on polarization of pump beam. Dye radiation vertically polarized (laboratory frame), as was the initial pump polarization. The solid line represents the fitted curve.

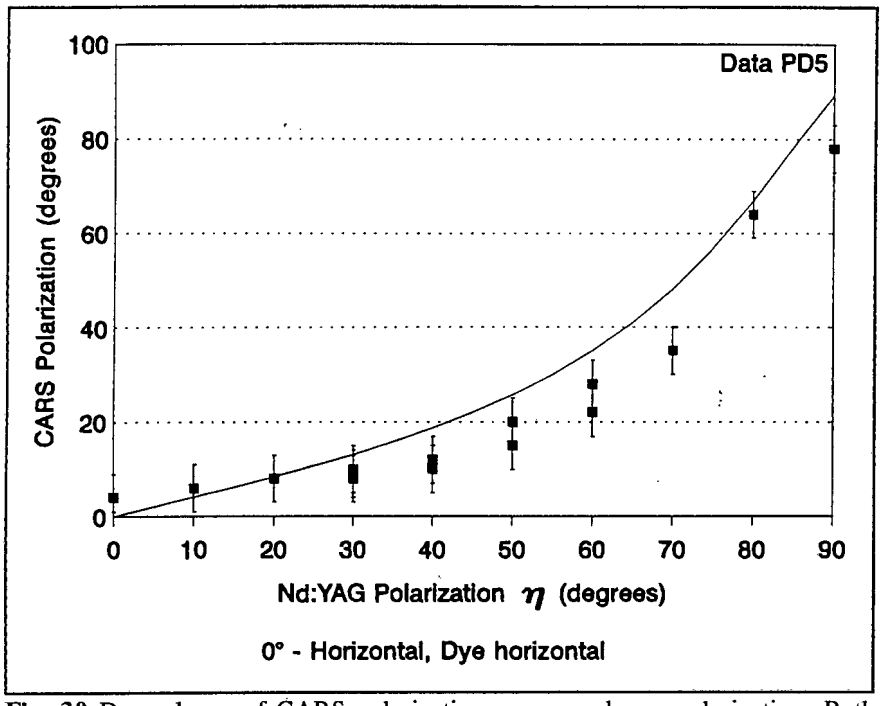

Fig. 30 Dependence of CARS polarization on pump beam polarization. Both pump and dye beams initially horizontally polarized. The curve uses the average χ_{ratio} parameter from PD1-PD4.

From the theoretical curves fitted to the data, we were able to determine the ratio of the two susceptibility components. This ratio with its related uncertainty is listed in Table 3.

Table 3 : Ratio of $\chi^{(3)}$ components

Data set	$\frac{\chi_{abba}}{\chi_{abab}}$	Uncertainty (standard deviation)
PD1	0.810	0.259
PD2	1.030	0.278
PD3	0.760	0.281
PD4	0.833	0.083

The four estimates for the ratio of the non-vanishing $\chi^{(3)}$ components agree reasonable well with each other. In particular, the two types of related yet distinct experiments performed i.e. measuring the CARS signal intensity (PD1 - PD4) as opposed to its polarization (PD5), produced similar results. This can be seen by the good fit of the PD5 data to its theoretical curve, where the average of the χ_{abba}/χ_{abab} values, 0.858 has been used. The standard deviation of this average is 0.118. This is an average over all polarizations conditions, rather

than at any specific laser polarization state, since these ratios were determined by curve-fitting to polarization dependent data. However, since the electric susceptibility is a bulk property of the diamond, its components should be independent of the input beams polarization.

Chapter 5
Conclusion

Our investigations into Coherent Anti-Stokes Raman Scattering of diamond, has revealed much about the CARS technique in general. Aspects investigated include the need for phase matching, various intensity dependencies, and polarization studies which provide relative susceptibility component information. The study of the phase matching requirement was made possible due to diamond's high index of refraction and significant dispersion. This necessity for phase matching of the input electric fields was thoroughly researched, and confirmed the $sinc^2$ nature on the phase mismatch of the laser beams. The CARS signal intensity falls off rapidly, as the beams are moved off from the perfect crossing angle $\sim 1.5°$.

The theoretical dependence of the CARS intensity, in a linear fashion on the Stokes dye laser intensity, and as the square of the pump Nd:YAG intensity, was experimentally established. Polarization studies revealed the intuitive prediction that the polarization of the CARS signal, with the dye laser polarization kept constant, followed that of the pump Nd:YAG beam though this was not a linear relationship. The ratio of the non-vanishing components of the cubic electric susceptibility, was obtained by fitting the expected curves to the intensity dependent polarization data.

The CARS spectral data confirmed the Raman shift of 1332 cm^{-1} for diamond. The CARS linewidth was also found to be the same as that for the spontaneous Raman line, namely 1.2 cm^{-1} (HWHM). The theoretical CARS lineshape was fitted to the spectral data, through the combination of the Fast Fourier Transform and non-linear curve fitting Levenberg-Marquardt algorithms. The contribution of the non-resonant susceptibility constant background was found to be small, yet significant. This was shown by the good fit obtained

to the spectral data, when the non-resonant contribution itself was excluded from the assumed lineshape expression, while its role in the interference term was not. The ratio of the non-resonant to resonant susceptibility components 0.0278, also confirms the relative size of this background contribution.

The variation in some of the data points, and the lack of a perfect fit to the theoretical mismatch dependence, are as a result of the unknown relationship between the Nd:YAG and dye lasers. This relationship, in terms of both its temporal and spectral natures, needs to be investigated, as this would allow a complete and thorough analysis of any measured CARS signal.

Various experimental designs were considered, each with its own advantage and disadvantage. The simpler setups allowed a CARS signal to be easily generated, though this was of (relative) lower intensity and with no definite phase matching. Additional complexity of design was required to establish a unique phase matching angle, and optimal CARS signal intensity.

The inability to work with a complete solid state laser system was a disappointment. The expected large increase in the intensity of the CARS signal, is a great incentive to pursue Stimulated Raman Scattering in diamond. This would mean acquiring the use of a multi-mode laser in order to test our hypothesis on the faster gain threshold of Stimulated Brillouin Scattering.

Acknowledgements

I am grateful to my supervisors Professor Gerald Robertson and Professor Steve Driver, who have shared their knowledge, time and experience with me. Their continuous encouragement, patience, and approachable nature, made learning the methodology of research an enjoyable task. I have gained tremendously through my interaction with them and will always be grateful to them, especially for allowing me to "play" in their laboratory, for this has broadened the practical side of my knowledge, while being a lot of fun.

I am also indebted to Dr. Sisa Pityana, who gave up his own time to allow me to perform a large fraction of the (sometimes exhausting) experimental work, and whose encouragement got me through some of the more trying times. The many conversations we shared, were also most enlightening.

To Allan Hanbury, my colleague and friend, thanks must go firstly for writing the PLOP computer program. It was an invaluable tool in my own research, and I know in many of the other projects that have and will be performed in the Laser Laboratory. Thank you also for letting me learn some image processing from you, and for the long hours we spent in acquiring some knowledge in UNIX. I have enjoyed all the discussions we've had, in the time that I have inhabited the Lab. with you.

Mr. Danie Momsen, and his team in the Physics Workshop were always willing to help, and their friendly, prompt and professional attitude to their work, allowed my study to proceed without undue hesitation.

I have also been stimulated and assisted by many other students and lecturers within UCT's Physics department, and this together with the friendly attitude of the non-academic staff, made my stay at UCT most enjoyable.

Many thanks must also go to De Beers Industrial Diamonds (Pty.) Ltd., who have supported me financially over the last six years, and who allowed me to proceed with this degree while

providing material, financial and supervisory assistance for this work. In particular, Mr Gordon Taylor of De Beers was always ready to help, and took a keen interest in the progress we were making. His assistance in providing the diamonds, and advice in some of the experimental aspects, was invaluable.

I could have not have accomplished this work without the aid of my many friends, both in Cape Town and Johannesburg. They have fed and entertained me, lifted my spirits when I needed cheering up, allowed me the use of their computers to complete writing this thesis, and above all supported me by being my friends. No words can truly express my gratitude to them.

Finally, but most importantly, I will always be grateful for and indebted to my parents and brothers, who have continuously encouraged, motivated and supported me, even when they were unsure about my chosen profession. All my efforts are as much an acknowledgement to them as they are for my own benefit.

References

1. Raman C V, Krishnan K S, Nature, **121**, 501 (1928)

2. Maker P D and Terhune R W, Phys. Rev. **137**, A801 (1965)

3. Greenhalgh D A, Quantitative CARS Spectroscopy, Advances in Non-linear spectroscopy, vol. 15, Advances in Spectroscopy, edited by Clark R J H & Hester R E, John Wiley & Sons Ltd., England, 193-251 (1988)

4. Eckbreth A C, Bonczyk P A, Verdieck J K, Combustion Diagnostics by Laser Raman and Fluorescence Techniques, Progress in Energy and Combustion Science, **5**, 253-322 (1979)

5. Druet S A J and Taran J P E, CARS Spectroscopy, Progress in Quantum Electronics, **7**, 1-72 (1981)

6. Nibler J W and Pubanz G A, Coherent Raman Spectroscopy of Gases, Advances in Non-linear Spectroscopy, ed. Clark R.J.H. and Hester R.E., John Wiley & Sons Ltd., England, 1988

7. Levenson M D, Flytzanis C and Bloembergen N, Phys. Rev., **B 6**, 3962-3965 (1972)

8. Levenson M D and Bloembergen N, Phys. Rev., **B 10**, 4447 (1974)

9. Eesley G L, Coherent Raman Spectroscopy, Permagon Press, Oxford (1981)

10. Levenson M D and Kano S S, Non-linear Laser Spectroscopy, 2nd edn., Academic Press, New York (1988)

11. Maeda S, Kamisuki T, Adachi Y, Condensed Phase CARS, in Advances in Non-linear Spectroscopy, edited by Clark R J H & Hester R E , John Wiley & Sons Ltd., England (1988)

12. Bloembergen N, Recent progress in four-wave mixing spectroscopy in crystals, Light scattering in solids, ed. Birman J L, Cummins H Z, Rebane K K, Plenum Publishing, New York, 423-35 (1979)

13. Foggi P, Schettino V, Rivista del Nuovo Cimento, **15**, No. 7, 1-82 (1992)

14. Titkov S V, Zaytseva T M, Marfunin A S, Orlov R Yu, Izu. Akad. Nauk. Ser. Geol., No. 11, 157-9 (1992)

15. Nibler J W and Knighten G V, Coherent Raman Spectroscopy, Raman Spectroscopy of Gases and Liquids, ed. Weber A, Topics in Current Physics, vol. 3, Springer-Verlag, Heidelberg (1979)

16. Armstrong A J, Bloembergen N, Ducuing J, Pershan P S, Phys. Rev., **127**, 1918 (1962)

17. Boyd R W, Non-linear Optics, Academic Press, New York (1992)

18. Bloembergen N, Nonlinear Optics, Addison-Wesley Publishing, USA (1991)

19. Shen Y R, Principles of Non-linear Optics, Wiley, New York (1984)

20. Popov S V, Svirko Yu P, Zheludev N I, Susceptibility Tensors for Nonlinear Optics, Institute of Physics Publishing Ltd., Bristol (1995)

21. Nibler J W and Yang J J, Non-linear Raman Spectroscopy of Gases, Ann. Revs. Phys. Chem., **38**, 349-81 (1987)

22. Eckbreth A C, Applied Physics Letters, **32**, 421 (1978)

23. Kleinmann D A, Phys. Rev., **126**, 1977 (1962)

24. Hecht E, Optics, 2nd. edition, Addison-Wesley Publishing Company Inc., Massachusetts (1987)

25. Kelly A, Groves G W, Crystallography and Crystal Defects, Longman Group Limited, London (1970)

26. Burns G, Glazer A M, Space Groups for Solid State Scientists, Academic Press Inc., New York (1978)

27. Long D A, Raman Spectroscopy, McGraw-Hill, London (1977)

28. Solin S A, Ramdas A K, Phys. Rev., **B 1**, 1687 (1970)

29. McQuillan A K, Clements W R L, Stoicheff B P, Stimulated Raman Emission in Diamond: Spectrum, Gain and Angular Distribution of Intensity, Phys. Rev., **A 1**, 628-635 (1970)

30. Washington M A, Cummins H Z, Phys. Rev., **B 15**, 5840 (1977)

31. Gray W E, American Institute of Physics Handbook, McGraw-Hill Inc., New York (1972)

32. Lambda Physik laser dye wall-chart, (1983)

33. Ramdas A K, Raman and Brillouin scattering in diamond, Diamond Optics III, SPIE, **1325**, 17 - 28 (1990)

34. Lide D R, CRC Handbook of Chemistry and Physics, 74th edition, CRC Press Inc., Boca Rato (1993)

35. Anderson J, MSc. Thesis, University of Cape Town (1996)